# Ex-situ transferring of polydopamine films on semiconductor interface: Evidence of functional hybrid heterojunction

Jakub Szewczyk, Marcin Ziółek, Katarzyna Siuzdak, Igor Iatsunskyi, Mikolaj Pochylski, Daniel Aguilar-Ferrer, Mateusz Kempiński, Fida Tanos, Jacek Gapiński, Mikhael Bechelany, et al.

European Polymer Journal 206 (2024) 112781

Contents lists available at ScienceDirect

European Polymer Journal

journal homepage: www.elsevier.com/locate/europolj

# *Ex-situ* transferring of polydopamine films on semiconductor interface: Evidence of functional hybrid heterojunction

Jakub Szewczyk [a,b], Marcin Ziółek [c], Katarzyna Siuzdak [d], Igor Iatsunskyi [a], Mikołaj Pochylski [c], Daniel Aguilar-Ferrer [a,b], Mateusz Kempiński [c], Fida Tanos [b], Jacek Gapiński [c], Mikhael Bechelany [b,e], Emerson Coy [a,*]

[a] NanoBioMedical Centre, Adam Mickiewicz University, Wszechnicy Piastowskiej 3, 61-614 Poznan, Poland
[b] Institut Europeen des Membranes, IEM, UMR 5635, Univ Montpellier, ENSCM, CNRS, 34730 Montpellier, France
[c] Faculty of Physics, Adam Mickiewicz University, ul. Uniwersytet Poznańskiego 2, 61-614 Poznań, Poland
[d] Centre of Laser and Plasma Engineering, The Szewalski Institute of Fluid-Flow Machinery, Fiszera 14 Str., 80-231 Gdańsk, Poland
[e] Gulf University for Science and Technology, GUST, 32093 Hawally, Kuwait

ARTICLE INFO

*Keywords:*
Polydopamine
Functional surfaces
Interfaces
Electron transfer
Metal oxides
Photo degradation

ABSTRACT

Polydopamine (PDA) films, when combined with model nanometric semiconductor substrates like titanium dioxide ($TiO_2$) and zinc oxide (ZnO), enhance photocatalytic performance, generating a unique *ex-situ* functional heterojunction. We investigate PDA air/water films transferred onto large surfaces, revealing Janus-like films with strong chemical attachment. Spectroscopic methods confirm a functional hybrid heterojunction, while electrochemical studies show significant improvements with transfer resistance enhancement of ~2250 %. This opens doors to various practical applications for hybrid heterojunctions.

## 1. Introduction

Polydopamine (PDA) is a biomimetic material of constantly increasing interest since its discovery in 2007 [1]. Its biomimetic character comes from imitating the eumelanin-based biopolymer responsible for marine mussel adhesive properties [1–4]. One of the main advantages of this material is its straightforward production pathway, namely the autooxidation of dopamine in a solution of slightly basic pH [1,5] or electrodeposition of the PDA from the dopamine solution [6]. These are typical procedures for generating PDA nanoparticles [7,8] or functional PDA coating on various materials, resulting in all types of composites: 0D (0 dimensional) [9–12], 1D [13–18], 2D [19] and 3D [20,21]. It is worth noting that in the case of *in-situ* growth, the structure of the polymer depends on the substrate [22]. However, a breakthrough discovery was the observation of a free-standing polydopamine film generated at the air/water (a/w) interface during the autooxidation process [23]. [24,25]. Moreover, structures with 2D or 2D-like laminar features in these PDA a/w films were observed in a recent study [26]. Apparent similarities to graphite or graphene oxide materials have been shown using X-ray diffractometry (XRD) and Raman spectroscopy. Since no known synthetic pathway leads to such materials from dopamine solution, the hypothesis of a 2D-like supramolecular ordering of PDA is the most plausible scenario. Further studies have attempted to control the synthesis of the a/w films, aiming to produce thin, homogeneous and chemically pure films. As a result, high-quality material on a centimetre scale was obtained [27], and the production process seems to be easily scalable. Importantly, we have shown their superior mechanical strength and stability, allowing them to act easily as transferable free-standing films [28]. An additional fascinating aspect of the a/w films is the possible difference between the water and air-exposed surfaces, resembling Janus films or Janus membranes, as observed by Hong *et al.* in catecholamine microfilms from the air/water interface [29], however, no such studies have been performed for a/w PDA films so far, despite growing interest in the field of Janus films [30].

Another interesting aspect to investigate is the application potential of the a/w films in energy and remediation-related fields. For example, a recent review article discussed the application and perspectives of polydopamine-based composites for photocatalytic processes [31]. One of the most exciting applications in this field is the solar-driven photocatalytic decomposition of dyes and other chemical reagents for water remediation [32]. It has been shown that several disadvantages characterizing pure $TiO_2$, ZnO and other wide bandgap semiconductors e.g.

* Corresponding author.
*E-mail address:* coyeme@amu.edu.pl (E. Coy).

https://doi.org/10.1016/j.eurpolymj.2024.112781
Received 28 November 2023; Received in revised form 9 January 2024; Accepted 15 January 2024
Available online 21 January 2024

ZnS composites, could often be minimized or eliminated by modifying their surface with polydopamine, e.g. reduction of photoluminescence [33] decrease of the bandgap [34], increased effectiveness of transport and tunneling of charge carriers [14]an enhancement of the light absorption in vis range (redshift), and efficient separation of photogenerated charge carriers [35]. Finally- it was previously shown that the charge–discharge property of polydopamine induces electron backflow following the S-scheme heterojunction mechanism between $TiO_2$ and PDA. Briefly, the interfacial electron transfer (electron charge) occurs when the light is on, while the backflow of accumulated electrons from PDA to $TiO_2$ (electron discharge) happens when the light is turned off [36]. Nevertheless, these nanocomposites were obtained by direct polymerization of PDA in solution, and the effect of enhanced photocatalytic properties was mainly observed in nanoparticles, porous meshes and nanorods. No similar effect has been described for laminar nanocomposites based on PDA transferable films deposited on the photocatalyst surface. In general, the electronic properties of PDA nanomaterials are quite different from those of PDA/semiconductor interfaces, and the observed enhancement is often attributed to the *in-situ* polymerization and, possibly, to the quasi-ordinated growth of PDA on crystalline materials. Thus, the *ex-situ* growth of PDA films and the transfer of ready products on functional substrates might allow the exploitation of the properties of PDA/semiconductor interfaces in many fields. In this sense, there are many questions to be answered. For example, thin films of PDA grown *in-situ* (<5 nm) typically exhibit higher performance than thicker ones. Whereas PDA films from a/w, are an order of magnitude thicker (>15 nm) than their *in-situ* counterparts. Therefore, it is important to answer whether *ex-situ* transferring of fully polymerized PDA films onto functional substrates also results in photocatalytic enhancement. If so, How does it scale with achievable film thickness (>15 nm)? This would ultimately allow the proposal of a model for the light interaction at the polydopamine-inorganic semiconductor interface.

Taking it all into account, here we provide a comprehensive study of the following aspects: *i)* the differences between the chemical and physical properties of the upper and bottom surfaces of the laminar 2D-like thin PDA films from the air/water interface and their different application potential, *ii)* thickness dependence to evaluate its influence onto physicochemical and electrochemical properties and determine the most promising candidate for *ex-situ* transferring towards electrochemical experiments, *iii)* whether *ex-situ* transferred PDA films carry with them the previously observed photocatalytic enhancement, boosting the efficiency of photocatalytic degradation of the methylene blue (MB) in comparison to the $TiO_2$ thin films on a centimetre-scale. The latter is also an important application aspect because MB is a widely used dye in the textile industry. It is toxic, carcinogenic, and non-biodegradable and thus poses a health threat to living organisms [37]. Our results bring us closer to the practical application of relatively cheap and easy-to-obtain large-size materials for photocatalytic applications, e.g. organic pollutants degradation, an emerging topic [38–41].

## 2. Materials and methods

### 2.1. Chemical reagents

Materials of analytical purity level were used in all synthesis procedures without any further purifications. Dopamine hydrochloride (CAS: 62-31-7, s, >98 %), Trizma® base (CAS: 77–86-1, s, >99 %), Hydrochloric acid (CAS: 7647-01-0, l, 25 %), Diethylzinc (CAS: 557-20-0), Titanium tetrachloride (CAS: 7550-45-0), Sodium sulfate (CAS: 7757-82-6, s), Methylene Blue hydrate (CAS: 122965-43-9), Silicon wafer (Si 100, CAS: 7440-21-3, s), Quartz (fused, thickness: 1.0 mm) from Sigma-Aldrich and ultrapure deionized water from a Hydrolab Ultra UV system were used.

### 2.2. Synthesis of the polydopamine films

The synthesis of films was carried out in the optimised conditions determined in our previous work [27]. Dopamine (0.5 mg $ml^{-1}$) in the form of dopamine hydrochloride was added to a Petri dish (7.5 cm in diameter, 2 cm in height) containing Tris buffer solution (10 mmol, 45 mL). Stirring (300 RPM) took place on a magnetic plate throughout the whole synthesis time (10 and 24 h), and a glass lid covered the vessel with a small gap to allow air exchange. The purpose of using two different synthesis times was to obtain PDA a/w films of various thicknesses.

### 2.3. Transfer of the films

Two different transferring methods were applied to investigate both sides (surfaces) of the obtained films. By the use of the first procedure (scooping), the bottom surface of the film was in contact with a substrate, and the upper surface was exposed. Scooping is a simple procedure of immersing the substrate under the previously cut fragment of the floating film at a low angle (~30°) and withdrawing the substrate, utilizing gravity force to attach the film to the substrate, shown schematically in Fig. 1a. Although much less known than the Langmuir-blodgett technique, this method has several advantages, such as simplicity and lack of influence on the structure of the material [42]. Films transferred by employing this method will be denoted with the "sc" abbreviation. The stamping procedure seems much more elusive, and to the best of our knowledge, we applied it for the first time to transfer films from the water surface. Again, a fragment of the floating film is being cut, but the substrate is reversed upside down and slowly touches the film's upper surface. The film is adhesively attached to the substrate and can be detached from the water surface by lifting the "stamp". As shown in Fig. 1b, it is the bottom surface of the film that is exposed by using the stamping procedure. Films transferred by employing the stamping procedure will be denoted with the "st" abbreviation.

### 2.4. Substrates and coatings

Depending on the characterization method, different substrates were prepared, such as: bare Silicon (1 0 0) wafers, Si wafers covered by a thin (<100 nm) coating of $TiO_2$ or ZnO (denoted as $Si/TiO_2$ and Si/ZnO, respectively) and quartz glass covered by a thin (<100 nm) coating of $TiO_2$ (denoted as $Q/TiO_2$). $TiO_2$ and ZnO layers were deposited by the atomic layer deposition (ALD) method, which is described in detail elsewhere [43–45]. Thin amorphous films were deposited to obtain a continuous layer with low roughness [45]. For clarity, the differentiation and naming of the samples are summarised in Table S1.

### 2.5. Physico-chemical characterization

Water contact angle (θ) measurements were performed using SEO – Phoenix 300 Touch Automatic Contact Angle Analyzer equipped with the industrial zoom lens Navitar TV zoom 7000 and SurfaceWare software. The test was performed two times for each sample (for each group, there were four samples, so x8 tests for each group) by using 50 uL of deionized water. The result of each measurement is the average of 10 automatically determined values of the θ angle after t = 5 and 300 s. All structural characterization studies were performed on the polydopamine films obtained after 10 h and 24 h of oxidation, deposited on silicon Si (1 0 0) substrate using both transferring techniques and coded Si/PDA/10sc, Si/PDA/10st, Si/PDA/24sc and Si/PDA/24st, respectively. Grazing Incidence X-ray diffraction (GIXRD) characterization was executed with the use of an MRD-X'pert$^3$ diffractometer (PANalytical), operating at 45 kV and 40 mA with a Cu Kα radiation source (wavelength of 1.54 Å). Films were transferred via scooping or stamping onto clean Si wafers, dried and placed in the appropriate holders. Atomic Force Microscopy

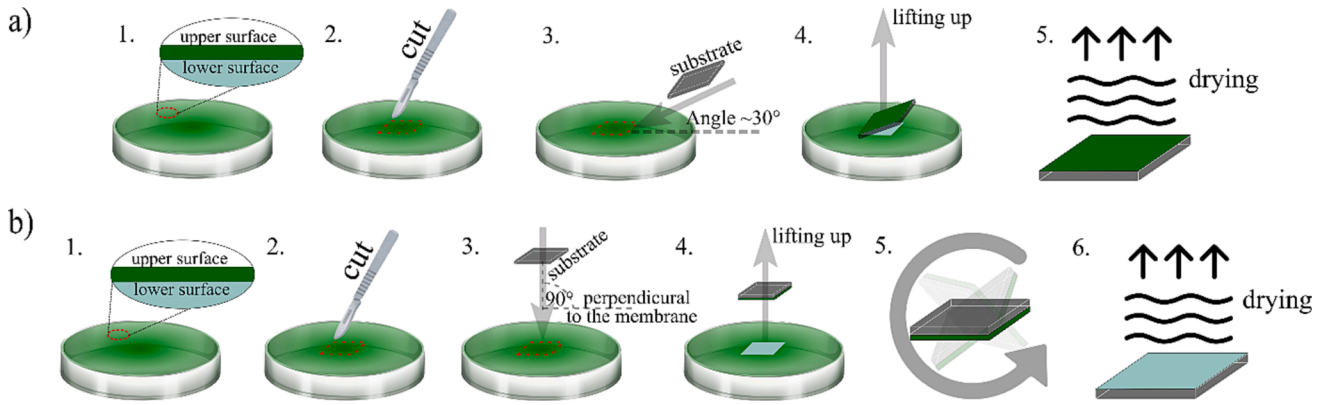


**Fig. 1.** Scheme of the (a) scooping (b) stamping transferring procedure.

measurements (AFM) were performed using an ICON–Bruker microscope. Complementary Gwyddion software was used for general height field and image processing, specifically for the analysis of profilometry data and thickness [46]. The thickness of films was determined from the average of 10 measurements on randomly selected sections crossing the crack in the film on which the substrate was exposed. The roughness was determined from the average of ten measurements of the root mean square (RMS) value in the area of 2 × 2 μm of the films. The roughness factor (*r*'), defined as the ratio between the actual and projected surface area, was appointed as the average of 10 measurements for each sample with the implemented functions of Gwyddion software. Raman Spectroscopy was performed using a Renishaw instrument equipped with microscope enclosure RE04, 633 nm laser source and Leica objective lens × 50. Exposure time was set to 1 s with 0.1 % of the power of the laser source (corresponding to 60 mW), and the number of accumulations was 10. Raman spectra of each sample are an average from 5 measurements in different areas. X-ray photoelectron spectroscopy (XPS) was performed using KRATOS:AXIS Ultra DLD, X-ray source: Al-Kalpha, 1486.6 eV - FWHM resolution 0.45 eV, acquisition time 0.1 s. High-resolution spectra of the regions corresponding to Si2p (112–92 eV), C1s (290–274 eV), O1s (540–520 eV) and N1s (408–390 eV) were investigated.

### 2.6. Spectroscopy and electrochemical studies

The room temperature stationary Photoluminescence (PL) properties of the bare and PDA-modified Si/ZnO were measured after excitation by IK Series Helium-Cadmium HeCd Laser Systems (325 nm) and collected by spectrometer Ocean Optics QE65 Pro. Stationary transmission UV–Vis spectroscopy was applied to investigate the bare and PDA-modified glass/$TiO_2$ bandgap using Ocean Optics DH-2000 Deuterium-Halogen lamp as a light source and Ocean Optics QE65 Pro Scientific-grade spectrometer. Obtained spectra of $TiO_2$ (an indirect band gap semiconductor) and ZnO (a direct band gap semiconductor) were transformed according to [47] and plotted against the photon energy. For transient absorption spectroscopic analysis of the bare and PDA-modified quartz/$TiO_2$ samples, a Helios spectrometer (Ultrafast Systems) and Spectra-Physics fs laser system were used. Measurements were performed in the spectral ranges of 300–900 nm and in the time range of up to 3 ns. Time evolution curves (kinetics) of differential absorption spectra were obtained. The excitation beam fell on the sample from the $TiO_2$ or PDA side. The pump pulses were set at 310 nm, and the pump pulse energy was 0.2, 1 and 5 μJ, corresponding to low, medium and high energy levels, respectively. Those energies correspond to energy densities between 100 and 2500 μJ $cm^{-2}$. To assign individual components of the decay signal, a mathematical fit was made, using the following function for the mixed first and second-order decay [48] $\Delta A(t) = \frac{An_0k_1}{k_1 exp(k_1(t-t_0))+n_0k_2(\exp(k_1(t-t_0))-1)}$ where $n_0$ is a dimensionless quantity proportional to the pump pulse energy, $A$ is relative absorbance, $t_0$ is the time of maximum $A$, and $k_1$, $k_2$ are first and second order decay rate constants, respectively. The superior or satisfactory fit was obtained for all presented kinetic curves, which is summarized in Table S3. The global analysis was performed to obtain wavelength-dependent amplitudes of the indicated time constants using Surface Explorer software from Ultrafast Systems, described in detail elsewhere [49]. All electrochemical studies were carried out using Autolab PGStat 302 N potentiostat–galvanostat systems (Metrohm, Autolab) in a three-electrode system where the investigated sample served as a working electrode, Pt-mesh as a counter electrode and Ag/AgCl/0.1 M KCl as a reference electrode in 0.5 M $Na_2SO_4$ electrolyte solution. Light sweep voltammetry (LSV) experiments were developed in a potential range from −0.7 to +1 V where the linear increase of potential was equal 10 mV/s, and the light/dark cycle length was 5 s. Two types of irradiation were used UV–vis and Vis. Cyclic amperometry (CA) experiments were developed during 300 s when the light/dark cycle length was equal to 5 s. Cyclic voltammetry (CV) experiments were developed from −1 to +1 V, where the increased potential speed was 50 mV/s. Electrochemical impedance spectroscopy (EIS) measurements were carried out in the range from 20 kHz to 0.1 Hz, where the amplitude was 10 mA. Before each measurement, 2 min conditioning time was ensured. The experiment was carried out in conditions without irradiation (dark) and when the working electrode was exposed to UV–vis and Vis radiation. The LV curves and EIS spectra were recorded in different light conditions using the solar simulator (Oriel), which was equipped with the optical filter to eliminate the radiation < 420 nm.

### 2.7. Photocatalytic performance

To evaluate the beneficial effect of the PDA a/w films deposition on the photocatalytic performance of the $TiO_2$ nanofilms, the experiment on the photocatalytic degradation of the methylene blue (MB) was planned. The concentrations of the MB solution were 2, 3 and 5 ppm, and it was stored in a Quartz cuvette of the volume 3 $cm^{3;}$ it was placed on a stirrer to allow the solution to mix during the experiment. The surface size of the catalyst was 1 $cm^2$. The photodegradation light source used in the experiment was a 300 W Xe arc lamp of Sciencetech's Tunable Light Source with 0.01 W $cm^{-2}$ intensity and a spectral range 300–1800 nm. A filter was set to cut out the infrared radiation - a quartz cuvette filled with distilled water. The experiments were run for 1 h, for the stability test experiment was run 4 times, including changing the solution with a new one every hour and using the same photocatalyst sample. A spectrum of the solution illuminated with Ocean Optics DH-2000 Halogen lamp was measured every 5 min and the decrease in the maximum absorbance of the UV–Vis spectra of the methylene blue (658 nm) was measured via Ocean Optics QE65 Pro Scientific-grade spectrometer. A photo of the cuvette with the photocatalyst placed in

it, the beam of light falling on its surface for driving photocatalytic degradation, and the perpendicularly mounted optical fiber directed to the spectrometer for recording the spectrum of the solution were shown in Fig. S1. Before and after the photodegradation experiment, the surface of the catalyst was examined via an optical microscope Keyence VHX 7100. The photograph of the MB solution before and after the photodegradation experiment was taken with a digital Xiaomi 50MP AI Quad Camera.

Additionally, methylene blue filtration efficiency was investigated on PVDF membrane filters (0.1 μm) and PDA/PVDF modified filters. The test was performed in a 10 mL omicon 8010 closed system under an applied pressure of 0.2 bar. Filtration efficiency was measured in the same manner as photodegradation efficiency.

## 3. Results and discussion

As indicated in Fig. 2, the work was divided into three steps. Firstly, polydopamine films were synthesized at the air/water interface using a previously optimized procedure (see section 2.2), and different procedures were applied to transfer films from the a/w interface on the surface of the Si(1 0 0) wafer, Si/$TiO_2$ and Si/ZnO (see section 2.3). The morphological, chemical and structural divergence resulting from varying dopamine oxidation time and transferring techniques were investigated with the use of the AFM, water contact angle measurements, XRD, Raman Spectroscopy, FTIR and XPS (see section 3.1). Next, within step II, thin $TiO_2$ and ZnO coatings were deposited on the Silicon substrate via ALD method, and the polymer was deposited on top using the most promising PDA transferring procedure. Finally, in the last step, we investigated the effect of the PDA/semiconductor interface on the optical and electrochemical properties and photocatalytic MB degradation efficiency (see section 3.2).

### 3.1. Morphological, chemical and structural properties

To investigate the influence of the transferring procedure and synthesis time on the thickness and roughness of the transferred PDA a/w films, Atomic force microscopy was applied. In Fig. 3a the box chart shows the results of film thickness obtained for the films transferred on three types of substrates- Si, Si/ZnO and Si/$TiO_2$. Regardless of the substrate type, the mean thickness of the films transferred after 10 and 24 h of the synthesis was ~17.5 and ~30 nm, respectively. Certainly, this is not a linear increment, which is consistent with the former studies suggesting a faster thickness increase in the first hours of synthesis [25,27]. Notably, the transferring procedure had a negligible influence on the film thickness obtained after 10 h growth (random variations), but after 24 h all the films transferred with the stamping procedure were significantly thicker than the scooping ones. We speculate that capillary forces and stretching of the films, which are more effective in the scooping procedure, might compress the films. Moreover, the chemical environment of both surfaces could play a role in their attachment and, therefore, their compression. In turn, the roughness (RMS) of the obtained composite surfaces clearly depends on the transferring procedure regardless of the growth time (Fig. 3b). For Si/ZnO and Si/$TiO_2$ samples, stamping resulted in higher roughness compared to scooping, in contrast to Si/PDA sample, where a reverse effect was found. We think the degree of hydrophobicity determines this c because the water contact angle on the bare Si is around 10° lower than on Si/ZnO and Si/$TiO_2$. That leads to the conclusion that the scooping technique is the best choice to maintain low film roughness after its transfer onto a more hydrophobic substrate. As previously reported, using the optimised synthesis conditions (stirring speed, pH, dopamine concentration) provides minimum achievable roughness of the PDA a/w film before transfer [27]. Interestingly, there is no significant influence of the thickness of the film on its roughness after transfer.

Water contact angle measurements estimated the wettability of the samples. Due to finite samples' surface roughness, the measured angles had to be corrected using the Wenzels equation with the $r'$ roughness parameter values taken from AFM results (see Supplementary Information for details). The results of direct measurements and the correction effects are shown in Table S2 of Supplementary Information. The final (true) values of water contact angles for all samples are shown in Fig. 3c-e. They are only slightly higher than the directly measured values, resulting from relatively small surface roughness and the respective correction. Three main observations can be made from the results of contact angle measurements: *i)* the same PDA film transferred on different substrates may reveal different hydrophilicity, *ii)*

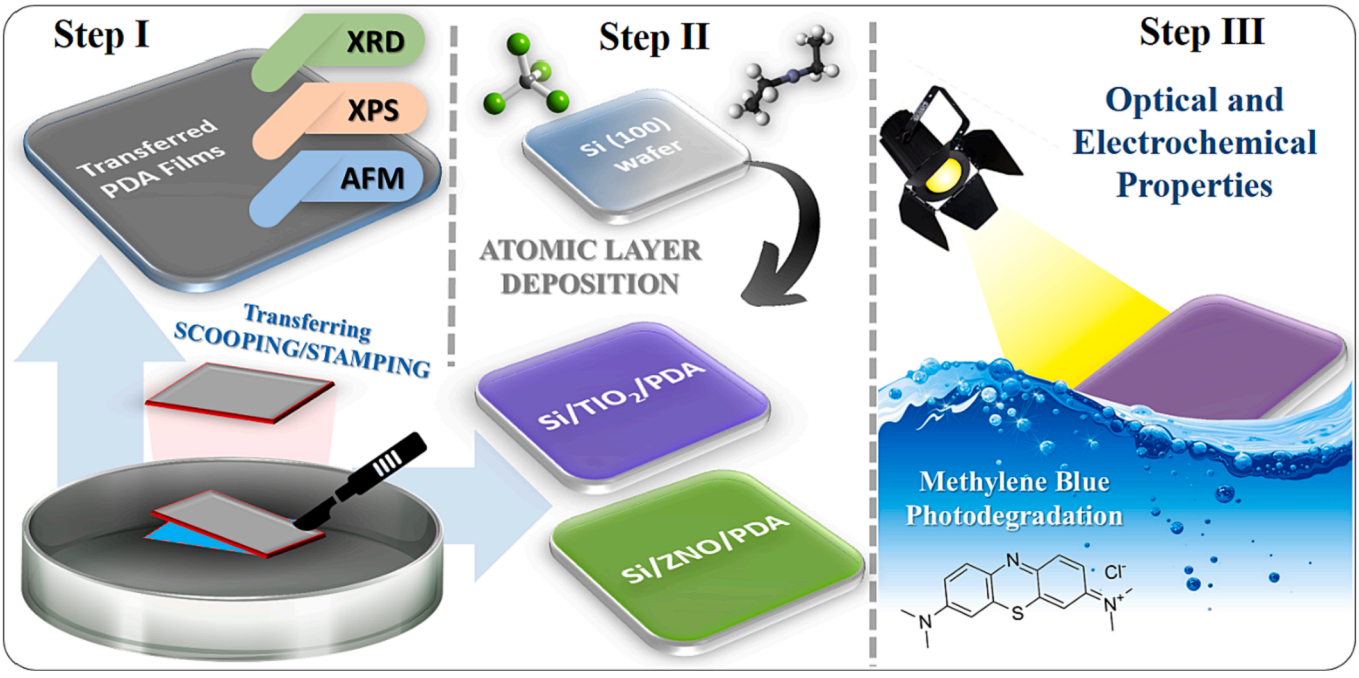


**Fig. 2.** Scheme of the workflow. We start with production and transfer of the PDA thin films, followed by their morphological, structural and chemical investigation before executing optical, electrochemical and photocatalytic experiments to investigate composites properties.

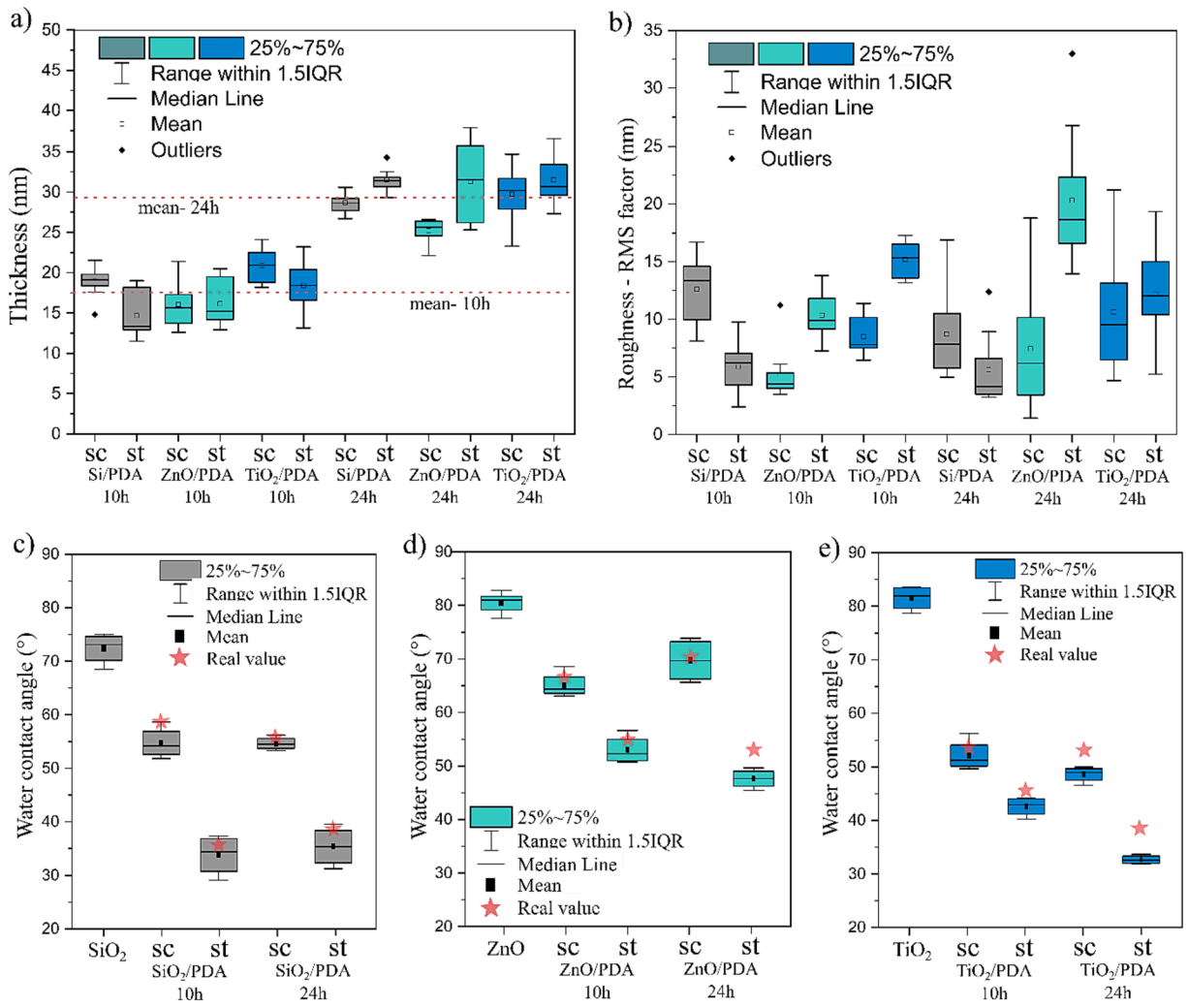


**Fig. 3.** (a) Thickness of the transferred PDA films on various substrates measured with AFM. (b) Roughness (RMS) of various samples surfaces measured with AFM. (c) Hydrophilic properties expressed by Water contact angle measurements before and after transfer of the PDA films on different substrates: Si, (d) Si/ZnO, (e) Si/$TiO_2$.

hydrophilicity of transferred films depends on film growth time, and *iii)* scooping and stamping identical films transferred onto identical supports have different water contact angles (scooping always higher). All these findings are very interesting. The first one confirms that the interaction of the substrate surface with the PDA film modifies the film properties. Si/PDA and $TiO_2$/PDA samples seem to be quite similar, especially for the film grown for 24 h, but the ZnO/PDA samples are much more hydrophobic. The hydrophilicity of polymers is complex, but one of the most important factors is surface energy [50]. The question arises: what is the reason for the lower surface energy of the PDA/ZnO interface? All substrates- acidic $SiO_2$, amphiphilic $TiO_2$ and ZnO- can accept electrons from electron-donating PDA catechol groups at the interface [51,52]. Probably due to the fewer adsorption sites on the ZnO surface, less electron-donor interaction occurs, affecting electron transfer through the interface [53]. This will be investigated later in the article. The second finding suggests that either the films change with the growth time or their interaction with the substrates depends on the film thickness or roughness. The third finding is very interesting because it provides a strong argument that the film is strongly asymmetric with regard to the chemical or structural composition of the bottom and top surfaces. During the self-assembly at the air/water interface, the hydrophilic parts of structural units building PDA films are directed toward the water to minimize the creation of a new interface and stabilize the structure [50,54,55]. Therefore, the stamping transferring method leads to more hydrophilic composites' surfaces (smaller water contact angle on the bottom surface). From Table S2 in the Supporting Information, we read that the difference between contact angles of the scooping and stamping samples equals 7.8° for Si/$TiO_2$/PDA/10, 14.3° for Si/$TiO_2$/PDA/24, 11.1° for Si/ZnO/PDA/10, 17.1° for Si/ZnO/PDA/24, 21.7° for Si/PDA/10, and 18.1° for Si/PDA/24. The AFM thickness and roughness data suggest that the bottom side of the PDA thin films is characterised by different chemical or structural arrangements, leading to a more hydrophilic character than the upper side, which was revealed by the water contact angle measurements. These chemical and structural divergences were investigated and described below. They show a clear picture, which, together with different hydrophilicity of the upper and lower side, suggest that we have obtained Janus PDA free-standing films.

Thanks to the discrete form of XRD spectra from crystalline substrates, the presence of a thin layer of the substrates can be detected and analyzed from XRD measurements. Especially if their characteristic peaks appear at angles different from those from the substrate and their crystalline phases are out-of-plane. We focus on the 2D-like structure of the films in different samples by evaluating their XRD data compared with the spectra from pure substrates (Fig. S2 of the Supplementary information).

Fig. 4a shows the results of such an experiment performed on the Si/PDA/24 samples (scooping and stamping). The peak at ~33.1° can be

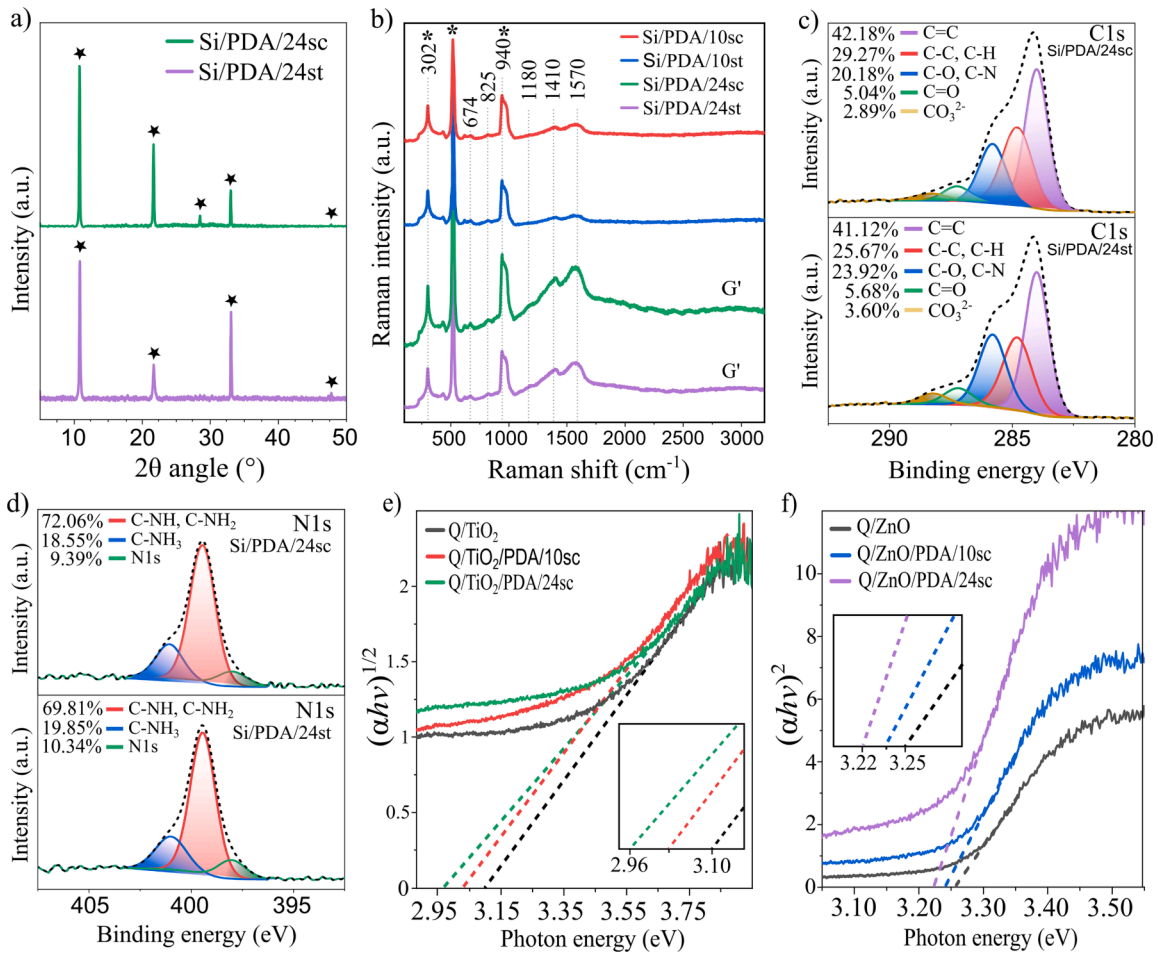


**Fig. 4.** (a) X-ray diffractogram of Si/PDA/24sc and Si/PDA/24st samples. (b) Raman spectra of Si/PDA/10sc, Si/PDA/10st, Si/PDA/24sc and Si/PDA/24st. The lines are shifted vertically for clarity. (c) X-ray photoelectron spectra for C1s region of the Si/PDA/24sc sample (upper) and Si/PDA/24st (lower), (d) N1s region of the Si/PDA/24sc sample (upper) and Si/PDA/24st (lower). (e) Transmission UV–Vis Tauc Plot of Quartz/$TiO_2$, Quartz/$TiO_2$/PDA/10sc, Quartz/$TiO_2$/PDA/24sc and samples, inset: zoom to photon energy 2.95–3.15 range. (f) Transmission UV–Vis Tauc Plot of Quartz/ZnO, Quartz/ZnO/PDA/10sc, Quartz/ZnO/PDA/24sc and samples, inset: zoom to photon energy 3.20–3.30 range.

assigned to both the substrate–silicon wafer [56] and part of the in-plane periodicity of PDA [57]. Therefore, it will be omitted from the analysis. In addition, the diffractograms for ZnO and $TiO_2$ coatings do not show any additional peaks, which confirms their assumed amorphous character (Fig. S2). The presence and positions of XRD peaks for Si/PDA/24 samples (Fig. 4a) suggest the presence of structural order resembling the ones found in 2D carbon-based materials, graphene oxide (~11°) and reduced graphene oxide (~22°) [58–61]. Moreover, the weak but noticeable diffraction peaks located near 47° may resemble peaks previously assigned to the (1 0 1) planes of graphite carbon [62–64], however, a similar peak is present in the spectrum of the pure Si substrate. Finally, there is a peak close to ~28° only in the scooping sample, originating most probably from the ordering similar to (0 0 2) face of graphitic crystals [65], indicating a more 2D-resembling structure.

The presence of certain chemical groups in Si/PDA samples was verified by means of Raman spectroscopy experiments (Fig. 4b). In all samples, the characteristic for carbonaceous materials peaks $sp^2$ can be observed: the D peak (~1410 $cm^{-1}$), which is attributed to structural defects in the hexagonal carbon lattice, and the G peak (~1570 $cm^{-1}$) linked with the in-plane vibration of the $sp^2$ carbon atoms [66–69]. There is a clear increase in these peaks intensity as the thickness of polydopamine films increases with the growth time, which is an expected observation and confirms the thickness differences as shown by the AFM method. Moreover, their intensity also slightly depends on the transferring method: it is lower for stamping. As the scattering signal comes from the whole membrane thickness present in the microscope confocal volume, this difference may originate either from membrane compression/expansion specific for its orientation-dependent interaction with the substrate or from the reduction of the number of freely oscillating carbon bonds due to the contact of the upper PDA surface with the silicon substrate. The $I_D/I_G$ ratio was also calculated, which was used to assess the disorder level of the graphene-like structure. The slight differences 0.916 for Si/PDA/10sc, 0.922 for Si/PDA/10st, 0.914 for Si/PDA/24sc, and 0.913 for Si/PDA/24st do not indicate any trend. However, thanks to the appropriate laser wavelength (633 nm) and relatively high energy used, the lower part of the spectrum (below 1000 $cm^{-1}$) can provide more information about the structural disorder employing the double-resonance (DR) Raman scattering mechanism [70,71]. Weak yet significant characteristic bands assigned to layer breathing vibrations (~825 $cm^{-1}$) were revealed [72], resembling the ones characteristic of defective and twisted carbons [71–73]. The peak at the wavenumber ~940 $cm^{-1}$ indicates that the C–H and/or O–H out-of-plane deformations [60] are significantly stronger compared to previous studies [27].

Similarly to the band around 302 $cm^{-1}$, it can be observed in the spectrum of pure Si subjected to the cleaning procedure in acetone and ethanol (Fig. S3), so they probably come from Si-H and Si-O bonds on the silicon surface. Another important observation is the presence of the ~1180 $cm^{-1}$ band, which is assigned to the NH in-plane deformation mode originating from the pyrrole ring in PDA structure [74], but it is

only visible for samples from the 24-hour series. The peak located at 674 $cm^{-1}$ originates from the stretching and deformation of aromatic rings [70] and remains visible in all samples, as these rings are the basic building blocks of PDA [75].

The position of 2D (G′) peak (for Si/PDA/24sc and Si/PDA/24st samples) is shifted towards higher wavenumbers in comparison to previous studies of thicker PDA a/w films [27]. As this type of shift is characteristic of PDA-based samples with lower oxygen content [76], it should be concluded that this is related to the oxidation time of dopamine. For much thinner Si/PDA/10 samples, 2D peak is very weak due to the much smaller scattering volume of these films and presumably, it is further shifting towards higher wavenumbers.

FTIR spectroscopy of the Si/PDA/24sc sample was performed to further confirm the chemical nature of the obtained polymer (Fig. S4). The broad band at 3190 $cm^{-1}$ indicates the presence of the hydroxyl and N–H groups [77]. At 1640 $cm^{-1}$ - The bending vibration peak of N–H [77] overlaps with C=O band [78]. Bands at 1300 $cm^{-1}$ and 1500 $cm^{-1}$ were assigned to C–O bonds and C=C ring stretching, respectively [77,78]. Finally, the strong absorption band at 1105 $cm^{-1}$ originates from Si-O bonds (PDA-substrate through catechol groups or native $SiO_2$ on Si substrate surface) [79].

To fully understand the difference between the top/and bottom faces of the PDA films, we performed XPS measurements, as shown in Fig. 4c and d. To properly understand the XPS results, it is important to remark that native oxide was not removed from the Si substrates (Fig. S3). Furthermore, it is important to keep in mind that other peaks originating from Silicon are visible at the Si2p spectrum of all PDA-deposited samples (Si-O), indicating the presence of the silane moieties (Figs. S5, S6, S7 and S8) [80], which proves the fact of binding of functional groups present in polydopamine to the silicon substrate. Importantly, the Si-O component has the largest share of the spectrum for the Si/PDA/10sc sample, followed by the Si/PDA/24sc. The stamping samples have a lower share of this component, which may indicate a weaker bond to the Si substrate. Due to the low penetration depth of the coating in the XPS test, the Si-O component is higher for thinner PDA layers in Si/PDA/10sc than for thicker one in Si/PDA/24sc. Furthermore, considering the C1s spectrum (Fig. 4c), there is a minor yet significant advantage in the $sp^2$ bonded carbons (C=C) subpeak area for scooping samples compared to the stamping, suggesting a more significant proportion of $sp^2$ hybridization rings in the structure of the obtained material. Nevertheless, the C–C and C–H bonds are related to $sp^3$ carbon, implying the presence of branched chains not subjected to pure 2D symmetry [81]. The presence of C–O and C=O subpeaks suggests that both catechol and quinone functional groups are formed, thus confirming the obtained PDA structure [82].

The C-NH and C-$NH_2$ peaks in the N1s spectrum (Fig. 4d), representing the final and intermediate dopamine oxidation products, are slightly stronger for the scooping samples. In turn, C-$NH_3$ most probably represents the protonated amino group (–$NH_3^+$) which is expected in basic pH as side chains contain nitrogen and resemble ammonia [81]. This component level is higher for stamping samples, which may be a result of the impurities contribution. The C1s, N1s and O1s spectra for the pure Si substrate and the Si/PDA/10 samples are presented in supplementary info (Figs. S3-S7).

### 3.2. Optical, photocatalytic and electrochemical properties

To investigate the influence of PDA films (particularly the method of transferring) on the semiconductor's optical properties, especially the bandgap value, UV–vis transmission spectroscopic measurements were carried out. Fig. 4e and 4f show Tauc Plots for $TiO_2$ and ZnO, respectively. The plots are compared with bare metal oxides and PDA samples of different thicknesses. For both experiments, the introduction of PDA24sc film showed a greater impact on the bandgap value, shifting it by 0.14 eV ($TiO_2$) and 0.03 eV (ZnO) towards lower photon energy. This effect is of minor importance for ZnO, because such a small shift cannot significantly affect the optical and photocatalytic properties of the material, although it remains consistent with the effect observed in ZnO NWs (~0.1 eV) [34]. However, thanks to a significant shift after deposition of the PDA, $TiO_2$ can exploit a part of the Vis spectrum (blue region of irradiation) for photocatalytic reactions. The presence of PDA10sc film also induces a smaller value shift, around 0.08 eV. Nevertheless, the possible mechanism was investigated using the transient absorption spectroscopy method described later in this section. To confirm whether the observed change in the bandgap energy value is not a result of the stationary absorption effect, Fig. S9 shows the measured absorbance spectra for the samples with $TiO_2$ and PDA. As it can be seen, a thin PDA film does not dramatically increase the absorption of radiation in the investigated spectrum, which is advantageous because most of the radiation can reach the surface of the semiconductor/PDA interface.

Fig. 5a presents the photoluminescence spectrum for bare Si/ZnO substrate and samples of different thicknesses and transferring techniques of the PDA films onto Si/ZnO. This substrate was selected because ZnO-based nanostructures are known for their photoluminescent properties [83], which reduces their suitability as photocatalysts [34]. The ZnO bright UV emission (near-band emission, NBE) is close to its absorption edge and produced by excitonic or band-band recombination [84]. Focusing on the literature reports, the room-temperature PL spectrum of ZnO is dominated by the free-exciton longitudinal optical (LO) phonon replica emissions [83,85]. This effect – exciton-phonon coupling – affects the stability of excitons [86]. In Fig. 5a, the position and intensity of the single NBE peak differ for various samples. As PDA shows significant light absorption in the UV region, the bands' intensity was normalized to compare their maximum positions (inset in Fig. 5a) [87]. A significant shift of the maximum of the peak towards higher photon-energy should be noted. It is ~0.03 and ~0.06 eV for thinner (10 h) and thicker (24 h) PDA films, respectively. Although it was found that the crystalline size ($d_{size}$) of the ZnO nanostructures greatly influences the photon energy of the emission peak [86], this cannot explain the shift observed in our experiment since the deposition of the PDA film could not affect the crystalline size of the ZnO. Instead, we postulate that the PDA coating increases energy required for electron–phonon recombination, which positively affects the stability of excitons in ZnO nanostructures.

In turn, deep-level emissions (DLE) in the visible-NIR range (from 3.1 eV to 1.653 eV) originate from crystalline defects and different film stoichiometry (Fig. 5 b and c), indicating the low ZnO's surface thermodynamic stability [88]. Three major types of emission can be distinguished, namely: green (2.19–2.48 eV), yellow-orange (1.98–2.19 eV), and red (1.65–1.98 eV) [84,89]. The differences in emission energies originate from different defect-related transitions. Orange and red luminescence bands that were observed in our experiment are assigned to oxygen interstitials ($O_i$) [90–93]. Deconvolution of the spectra showed that the functionalization of the surface with PDA film, compared to ZnO itself, must have influenced the concentration of defects, as it significantly quenched the appearance of bands close to 1.70 and 1.91 eV. Note that in the Fig. 5 b-c, the area under the peaks (a.u.) was embedded at each peak. It can also be concluded that the thicker the PDA coating (and thus the longer oxidation time), the stronger the effect. In turn, the band at ~2.15 eV is ascribed to the transition of an electron from the conduction band to deeply trapped holes in the oxygen interstitials [93–95]. The surface functionalization with a thin film of PDA did not significantly affect this type of emission. In short, polydopamine, with a high degree of oxidation by bonding through functional groups, had a positive effect on stoichiometry and the reduction of ZnO surface defects, contributing to the increase of its stability.

To measure the excitation's photogenerated excited state absorption energies and associated lifetimes, the time evolutions of differential absorption changes (kinetics) were obtained (Fig. 6a–c). Transient absorption changes were measured upon excitation at 310 nm for the samples with $TiO_2$ on quartz (to avoid direct excitation of the substrate

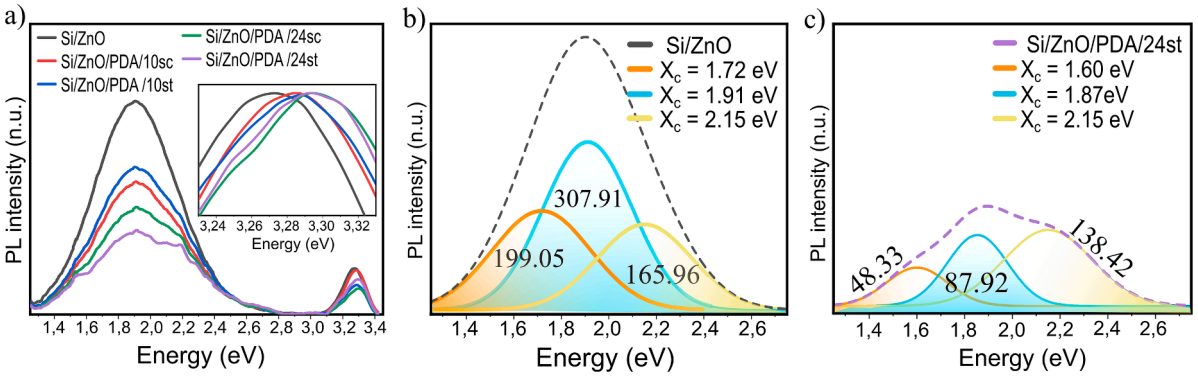


**Fig. 5.** (a) Photoluminescence spectra of the bare Si/ZnO and after deposition of PDA films. Inset: zoom to the NBE region, normalized. (b) PL spectra broadband in the visible- NIR range deconvoluted for bare Si/ZnO and (c) Si/ZnO/PDA/24st.

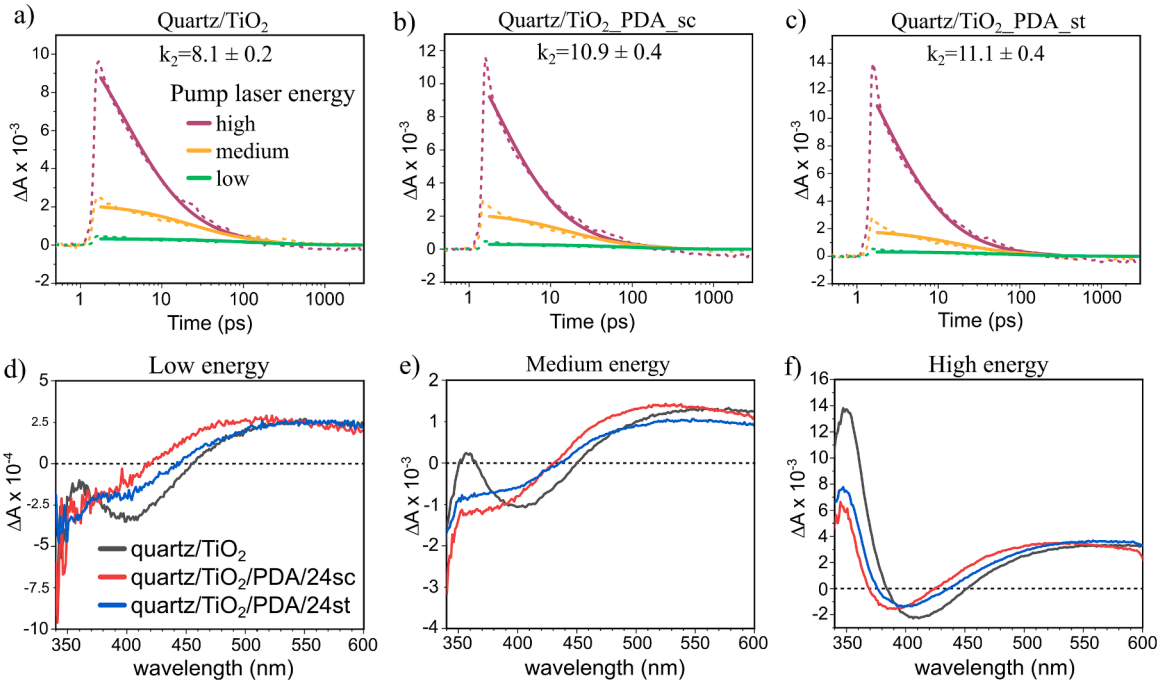


**Fig. 6.** (a) Representative emission decay traces for Q/$TiO_2$, (b) Q /$TiO_2$/PDA/24sc, (c) Q /$TiO_2$/PDA/24st. (d) Representative transient absorption spectra for a 10 ps time delay between pump and probe pulses for low energy, (e) medium energy, (f) high energy.

with UV irradiation). Kinetics at 590 nm (Fig. 6a-c) represent the decay of the population of holes in $TiO_2$ [48]. No signals from PDA alone or quartz alone were observed. The excitation from either the coating or the quartz side allows selective probing of different interfaces due to the small penetration depth of $TiO_2$ at the excitation wavelength of 310 nm. The kinetics were fitted with mixed first and second-order decay functions (Table S3). This model does not take into account the charge diffusion component, but high $R^2$ values and more or less constant values of $A$ for different pump pulse energies are strong evidence of a good fit of the model (Table S3). For all samples and both excitation sides, a dominant share is of the second-order decay, even for the lowest pump pulse energies. The values of the first-order rate constant ($k_1$) are either very small compared to the temporal range of the experiment or fitted with high relative error (reaching 100 %) for all samples; therefore, no conclusions can be drawn. When excited from the quartz side, similar radiative, second-order recombination rate constant ($k_2$) values are observed for the samples with and without PDA. On the contrary, when excited from the coating side, the constant rate $k_2$ is higher for samples with PDA sc and PDA st of about 35 % and 37 %, respectively (Table S3 and Fig. 6a–c), than that for the control samples with only $TiO_2$. This proves that PDA indeed affects the properties of $TiO_2$ close to its interface. Possible reasons for these significant differences will be discussed later in this paragraph. Importantly, a shorter excitation lifetime does not necessarily mean inferior photocatalytic properties. It was previously shown that despite the almost 10 times slower recombination kinetics of rutile than anatase, the photoactivity and catalytic properties of rutile were lower due to the deficit of surface electron holes [96]. It can also be noted that strong second-order recombination conditions are usually not fulfilled at typical sunlight intensities for photocatalysis but rather observed only with laser pulses.

For easy comparison, the spectrum at 10 ps after excitation was plotted to investigate trapped species contribution, and for clarity, spectra were presented in the range 320–600 nm in Fig. 6 d-f. It was previously reported that due to relaxation through deep sites, absorption bands in the transient absorption spectra of $TiO_2$ shift towards blue as deeply trapped carriers absorb photons of shorter wavelengths [97–99]. Oxygen vacancies ($V_{ox}$) can induce shallow defects when the thermodynamic effects of the structural relaxation are taken into account

[100–102]. Perhaps PDA passivates oxygen deficiency, which may affect the surface charge properties of the $TiO_2$ [103].

For a deeper analysis of the previously described kinetic differences, global fitting was performed using the approximation of the two-exponential plus constant offset function. Pre-exponential factor spectra of the components $\tau_1$ and $\tau_2$, that is, the amplitude spectra associated with the individual fitted time constants, were plotted along with the constant offset (const. offset), which stands for constant component, i.e. the final spectrum after 3 ns (Fig. S10). On the one hand, it was found that each decay curve has a fast component of a time constant between 0.86 and 6.1 ps standing for quenching of the photogenerated electrons (e.g. transfer, recombination or trapping). Note that for samples illuminated from the coating side, regardless of the energy used, this component is always faster for PDA-coated samples, as the heterojunction boosts the transfer of electrons from $TiO_2$ conduction band to PDA through the π-conjugated structure and functional groups. A slow component with a time constant between 14 and 230 ps is standing for the relaxation of trapped electrons. Further analyzing the spectra, we notice that samples with PDA (measured from the PDA side) show a smaller and shorter-wave share of the negative signal, which in samples with $TiO_2$ alone stretches up to ~500 nm. This signal may come from the steady-state absorption of the trap states in $TiO_2$ [104–106]. The method of PDA deposition is of little importance for this effect. In turn, the strong signal with a maximum of 340–350 nm, originating most probably from the direct hot transition in $TiO_2$ [48], is decreased for PDA- coated samples, which may indicate that local heating at the interface is lowered due to heterojunction. This is most probably caused by the difference in trapped holes ($O^-$) concentration, as postulated above [104]. The above differences around 350 nm for the $TiO_2$ samples with and without PDA can also be noticed in the transient absorption spectra at 10 ps (Fig. 6 d–f).

Considering all the previously obtained results, PDA films from group 24sc were selected as the most promising and they were subjected to electrochemical tests after deposition onto Si/$TiO_2$ and Si/ZnO. Cyclic Voltammograms of Si/ZnO/PDA (Fig. 7a) and Si/$TiO_2$/PDA (Fig. S11) indicate an increase in reduction peak in the cathodic regime; this is a promising indicator of the positive performance impact of PDA-modified composites compared to pure inorganic semiconductors. Next, the linear sweep voltammograms were generated by measurements under chopped illumination of visible (Fig. 7b) and UV–vis (Fig. S12a) light, showing higher photocurrent density (PD) for the $TiO_2$ samples with deposited PDA films in negative and positive potentials range. For ZnO, a positive effect can be seen for the VIS light illumination (Fig. S12b) and, partially, for the UV–vis illumination experiment (Fig. S12c). This experiment provides information on the photoelectrochemical activity of samples and shows that PDA enhances efficient charge separation, generating functional heterojunction, thus reducing electron-hole recombination.

The results of the EIS measurements are presented in Fig. 7c and d, where the significant influence of PDA on the curves can be seen. To analyze this effect, a fitting procedure (Table S4) and equivalent electric circuits (Fig.s S13 and S14) have been proposed and described in detail in the supplementary information (see pages S16-S21). Firstly, the models show that the real part of the impedance is higher for both $TiO_2$ and ZnO without irradiation (dark) and under the influence of light in the visible range. On the other hand, it decreases under the influence of UV–vis radiation. This indicates the correctness of the models and is fully in line with the theoretical assumptions, as both $TiO_2$ and ZnO are active in the UV range and not active in the visible range. More importantly, PDA greatly impacts the decrease in the real impedance component, representing charge transfer resistance. The mentioned decrease is reaching an extremely high value, especially for $TiO_2$, i.e. ~1920 % (dark), ~1080 % (UV–vis) and ~2250 % (Vis) in comparison to bare $TiO_2$. This is a higher result than previously described in the literature ~613 % (dark) for *in-situ* deposited PDA on $TiO_2$ nanorods [107]. Simultaneously, the results obtained for ZnO/PDA are also very promising. It is a 310 % (dark), 215 % (UV–Vis) and 216 % (Vis) decrease in comparison to bare ZnO. The most important result obtained in the present experiment proves that thin PDA films have particularly favorable photoactive properties (in a wide range from UV to Vis), but are also electrochemical (dark- no irradiation), positively influencing the electrochemical performance of inorganic semiconductor materials.

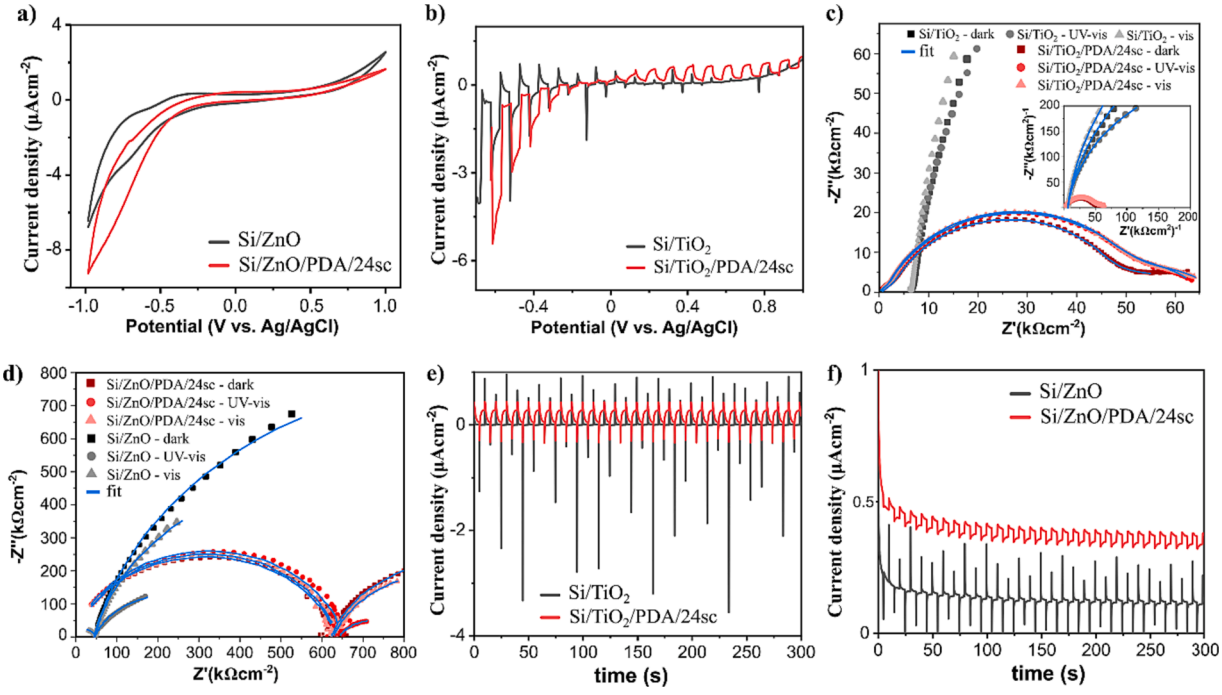


**Fig. 7.** (a) Cyclic voltammogram of Si/ZnO and Si/ZnO/PDA/24sc samples. (b) Light sweep voltammogram of Si/$TiO_2$ and Si/$TiO_2$/PDA/24sc samples under vis irradiation c) Electrochemical impedance spectra under different irradiation conditions of Si/$TiO_2$, Si/$TiO_2$/PDA/24sc, (d) Si/ZnO and Si/ZnO/PDA/24sc samples. (e) Cyclic light sweep amperometry under vis irradiation of Si/$TiO_2$, Si/$TiO_2$/PDA/24sc, (f) Si/ZnO and Si/ZnO/PDA/24sc samples.

However, the model of $TiO_2$/PDA taking into account charge transfer resistance at the PDA/electrolyte interphase (Fig. S12) indicates that the irradiation (vis and UV–Vis range) reduces impedance by ~60 % in comparison to dark conditions. In this case, a significant influence of irradiation is of great importance.

The *j–t* graphs for $TiO_2$ (Fig. 7e) and ZnO (Fig. 7f) show the amperometric response for the visible light on/off cycles. A significant contribution from the pyroelectric potential indicated by the sharp peaks (spikes) is visible. The pyro-phototronic effect was described in detail elsewhere [108–110]. It originates from the nanosecond-scale process of vis light-induced rapid temperature increase [109], as it was previously described that coupling of light and cooling of the device could enhance photocurrent stability [111]. Within this process, a charge carrier transport across the heterojunction is enhanced; hence, numerous recombinations occur, and a transient high output current is observed. After a short time, the photocurrent is stabilized due to the relatively slow photoexcitation process in comparison to trap states induced leakage current [109,112]. PDA caused a significant reduction in the intensity of these spikes, flattening the photocurrent density chart, which is further evidence of its positive effect on reducing the charge carrier's recombination rate [111]. Oxygen vacancy in amorphous $TiO_2$ could promote hole conduction by providing a "leaky" channel [113]. The oxygen vacancy defects in the amorphous ZnO films and their contribution to hole conduction were also reported [114]. Therefore, considering the amperometric responses of $TiO_2$/PDA and ZnO/PDA, we postulate that oxygen deficiency at the surface was modified by PDA film. The low photocurrent density was caused by the poor contact electrical contact with $TiO_2$ or ZnO, but in consistency with literature reports, polydopamine modification contributed to an increase in its value through efficient electron extraction [115].

Finally, the photocatalytic degradation of the methylene blue efficiency was investigated, and the mechanism was drawn as follows. Light-induced generation of the electron ($e^-$) *hole* ($h^+$) pairs (1). Generation of the hydroxyl radical through the hole (2). The reaction of the MB with the hydroxyl radical, degradation of the methylene blue (2b). Alternatively, the generation of the superoxide radical (3) and the reaction of the MB with the superoxide radical, thus, degradation of the methylene blue (3b).

$$TiO_2 + hv \rightarrow h^+ + e^- (1)$$

$$h^+ + OH^- \rightarrow OH^\bullet (2a)$$

$$OH^\bullet + MB \rightarrow CO_2 + H_2O (2b)$$

$$O_2 + e^- \rightarrow O_2^{\bullet -} (3a)$$

$$O_2^{\bullet -} + MB \rightarrow CO_2 + H_2O (3b)$$

The results of the photodegradation test are shown in Fig. 8a (photodegradation efficiency) and Fig. S16 (optical digital photographs). After the deposition of the PDA a/w films, the photocatalytic performance of the $TiO_2$ was significantly enhanced beyond 14 % after 1 h. Moreover, this trend was maintained during the four stability test cycles (Fig. 8b). In subsequent cycles, the increase in efficiency was lower yet significant. In addition, the stability of the composites was evaluated by providing optical microscopy photographs of the surface of the samples before and after the test (after drying under normal conditions) presented in Fig. S17. An important factor is the kinetics of photodegradation, here, we determined the rate constants by fitting the results to the first-order mechanism (Fig. S18). For MB solution with a concentration of 2 ppm, the constant k was equal $9.2 \times 10^{-3} \pm 5 \times 10^{-4}$ and $5.2 \times 10^{-3} \pm 4 \times 10^{-4}$ for Si/$TiO_2$/PDA and Si/$TiO_2$ respectively. This corresponds to degradation rates (DR) 3.31 and 1.87 (ug $h^{-1}$ $cm^{-2}$), confirming significant $TiO_2$ photocatalytic performance improvement by *ex-situ* transfer of the polydopamine film. We developed additional tests to exclude the major influence of other effects like heat and MB adsorption on the PDA film. As can be seen in Fig. S19a, the photodegradation of the MB for the reference Si sample was 12.22 % after 1 h under UV–Vis. In turn, a filtration test was performed to investigate the possible adsorption of MB on PDA film (Fig. S19b). The filtration efficiency of the PVDF filter was slightly increased by modification with polydopamine by 12.45 %. Therefore, taking into account the large surface area of the filter (4.9 $cm^2$) and pressure-forced flux of molecules, the adsorption of MB at the PDA surface is a relatively minor effect. Next, we performed tests with scavengers to investigate the contribution of photogenerated electrons and electron holes in the photocatalytic decomposition of MB. The ethylenediaminetetraacetic acid (EDTA), p-benzoquinone (BQ) and isopropyl alcohol (IPA) were applied as h+, superoxide radicals and hydroxyl radicals scavengers, respectively. A significant decrease in process efficiency was noted for EDTA and BQ. Indicating a slight advantage of the share of electron holes over electrons (Fig. S20). A moderate decrease was noted for IPA since hydroxyl radicals are produced indirectly by $TiO_2$ and directly by PDA [116]. Small but noticeable degradation efficiency for the reference sample (Si substrate) is related to the absorption of the IR spectrum in the range of which Si(1 0 0) exhibits low photoactivity [117]. *Ex-situ* transfer of the polydopamine film onto $TiO_2$ surface enhances photocatalytic MB degradation efficiency. First, a bandgap energy value is lowered, leading to the broader light spectrum utilization in a photocatalytic reaction. Secondly, oxygen deficiency at the semiconductor materials surface is modified by PDA film, and shallow defects concentration is decreased, resulting in less probable electron-hole recombinations on the trap states. Generated heterojunction promotes charge transfer and separation. Finally, when presented to the water, the composite shows a more hydrophilic character in comparison to the bare $TiO_2$ surface, enabling more water molecules to reach the surface and undergo reactions of the hydroxyl radicals generation.

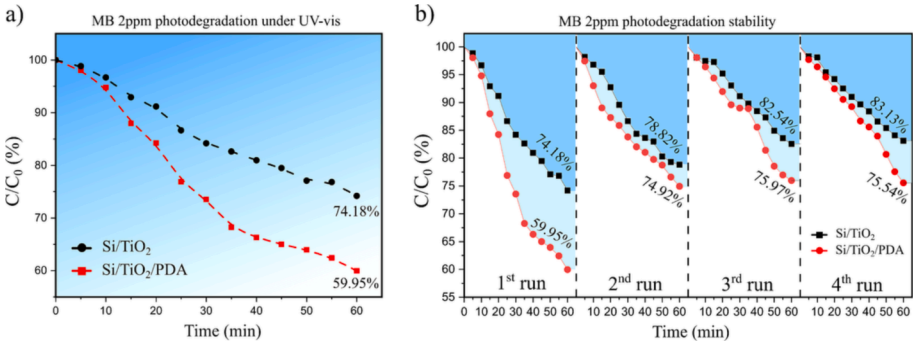


**Fig. 8.** (a) Graph of the photocatalytic degradation of the Methylene blue efficiency under UV–Vis light illumination. (b) Photocatalysts stability evaluation during 4 photocatalytic MB degradation cycles.

## 4. Conclusions

In summary, we successfully enhanced the ZnO and $TiO_2$ photocatalytic and photocatalytic-related properties using easy-transferable and centimetre-scale polydopamine films from the air/water interface. Starting from the previously developed optimised strategy, we prepared films of different thicknesses it is ~17.5 nm and ~30 nm. Next, have conclusively shown that PDA free-standing films can be successfully transferred on multiple functional substrates and resemble Janus structure with two distinct surfaces without losing the exceptional electronic properties observed in PDA/semiconductor interface in nanoparticles.

UV–Vis spectroscopy has shown a 0.14 eV bandgap value shift toward lower photon energies in $TiO_2$ thin coating using ~30 nm scooping PDA thin film. Photoluminescence spectroscopy has shown that PDA thin films are quenching the photoluminescence bands assigned to the oxygen defect-assisted recombinations in ZnO. Transient absorption spectroscopy in the femtosecond range provided insights into the mechanism of the enhancement of the electrical properties of the composites after PDA deposition by passivating the shallow defect states, boosting the electron transfer at the interface and lowering the local-heating effect in $TiO_2$ nanofilms. Finally, electrochemical studies were carried out. Most importantly, Electrochemical impedance spectroscopy revealed that PDA films have particularly favorable photoactive properties (in a wide range from UV to Vis), but are also purely electrochemical (dark- no irradiation). The postulated equivalent electrochemical circuit poses an exceptional drop in the charge transfer resistance component at the electrode/electrolyte interface after PDA deposition, reaching a ~2250 % drop for $TiO_2$ in Vis irradiation and ~310 % without irradiation for ZnO. Moreover, cyclic light sweep amperometry revealed a significant quenching of the pyro-phototronic effect, which in bare $TiO_2$ and ZnO originates from photogenerated electron-hole recombination. Further, the photocatalytic degradation of the methylene blue efficiency was investigated, and remarkable efficiency enhancement for the Si/$TiO_2$/PDA composite was noted, 14 % after 1 h in comparison to Si/$TiO_2$. Higher efficiency was also obtained in the subsequent four cycles. These benefits result from the creation of a functional organic/inorganic heterojunction.

Finally, although we have focused mainly on the photocatalytic aspects of such composites as a benchmarking of the transferring method, our findings can be easily applied to biomedicine, electronics and water remediation.

## CRediT authorship contribution statement

**Jakub Szewczyk:** Conceptualization, Data curation, Investigation, Methodology, Validation, Visualization, Writing – original draft, Writing – review & editing. **Marcin Ziółek:** Data curation, Investigation, Methodology, Validation, Writing – review & editing. **Katarzyna Siuzdak:** Data curation, Funding acquisition, Investigation, Methodology, Validation, Writing – review & editing. **Igor Iatsunskyi:** Investigation, Methodology, Validation, Writing – review & editing. **Mikołaj Pochylski:** Investigation, Methodology. **Daniel Aguilar-Ferrer:** Investigation, Methodology. **Mateusz Kempiński:** Investigation, Methodology. **Fida Tanos:** Investigation, Methodology. **Jacek Gapiński:** Methodology, Validation, Writing – review & editing. **Mikhael Bechelany:** Funding acquisition, Methodology, Resources, Supervision, Validation, Writing – review & editing. **Emerson Coy:** Conceptualization, Funding acquisition, Investigation, Methodology, Resources, Supervision, Validation, Writing – review & editing.

## Declaration of competing interest

The authors declare that they have no known competing financial interests or personal relationships that could have appeared to influence the work reported in this paper.

## Data availability

The raw/processed data required to reproduce these findings cannot be shared at this time as the data also forms part of an ongoing study. Data might be shared upon reasonable request to the corresponding author.

## Acknowledgments

The authors acknowledge the financial support from the National Science Centre of Poland (NCN) by the OPUS grant 2019/35/B/ST5/00248. This research was supported by a French Government Scholarship. J.S. is a scholarship holder of the Foundation of the Adam Mickiewicz University in Poznań for the academic year 2022/2023. K.S. acknowledges the partial financial support from the NCN Sonata-Bis 2017/26/E/ST5/00416 in the electrochemical section of this manuscript. Authors acknowledge as well the financial support of project H2020-MSCA-RISE-2017, 'Novel 1D photonic metal oxide nanostructures for early stage cancer detection' (Project number: 778157).

## Appendix A. Supplementary material

Supplementary data to this article can be found online at https://doi.org/10.1016/j.eurpolymj.2024.112781.

## References

[1] H. Lee, S.M. Dellatore, W.M. Miller, P.B. Messersmith, Mussel-inspired surface chemistry for multifunctional coatings, Science. 318 (2007) 426–430, https://doi.org/10.1126/science.1147241.
[2] L. Yang, S.L. Phua, J.K.H. Teo, C.L. Toh, S.K. Lau, J. Ma, X. Lu, A biomimetic approach to enhancing interfacial interactions: Polydopamine-coated clay as reinforcement for epoxy resin, ACS Appl. Mater. Interfaces. 3 (2011) 3026–3032, https://doi.org/10.1021/am200532j.
[3] T.G. Barclay, H.M. Hegab, S.R. Clarke, M. Ginic-Markovic, Versatile surface modification using polydopamine and related polycatecholamines: chemistry, structure, and applications, Adv. Mater. Interfaces. 4 (2017) 1601192, https://doi.org/10.1002/admi.201601192.
[4] G. Kafkopoulos, C.J. Padberg, J. Duvigneau, G.J. Vancso, Adhesion engineering in polymer-metal comolded joints with biomimetic polydopamine, ACS Appl. Mater. Interfaces. 13 (2021) 19244–19253, https://doi.org/10.1021/acsami.1c01070.
[5] J. Liebscher, Chemistry of polydopamine – scope, variation, and limitation, European J. Org. Chem. 2019 (2019) 4976–4994, https://doi.org/10.1002/ejoc.201900445.
[6] J. Szewczyk, D. Aguilar-Ferrer, E. Coy, Polydopamine films: Electrochemical growth and sensing applications, Eur. Polym. J. 174 (2022) 111346, https://doi.org/10.1016/j.eurpolymj.2022.111346.
[7] K. Żebrowska, E. Coy, K. Synoradzki, S. Jurga, P. Torruella, R. Mrówczyński, Facile and controllable growth of β-FeOOH nanostructures on polydopamine spheres, J. Phys. Chem. b. 124 (2020) 9456–9463, https://doi.org/10.1021/acs.jpcb.0c06627.
[8] C.C. Ho, S.J. Ding, The pH-controlled nanoparticles size of polydopamine for anticancer drug delivery, J. Mater. Sci. Mater. Med. 24 (2013) 2381–2390, https://doi.org/10.1007/s10856-013-4994-2.
[9] A. Jin, Y. Wang, K. Lin, L. Jiang, Nanoparticles modified by polydopamine: Working as "drug" carriers, Bioact. Mater. 5 (2020) 522–541, https://doi.org/10.1016/j.bioactmat.2020.04.003.
[10] R. Mrówczyński, A. Nan, R. Turcu, J. Leistner, J. Liebscher, Polydopamine - a versatile coating for surface-initiated ring-opening polymerization of lactide to polylactide, Macromol. Chem. Phys. 216 (2015) 211–217, https://doi.org/10.1002/macp.201400380.
[11] A. Petran, R. Mrówczyński, C. Filip, R. Turcu, J. Liebscher, Melanin-like polydopa amides-synthesis and application in functionalization of magnetic nanoparticles, Polym. Chem. 6 (2015) 2139–2149, https://doi.org/10.1039/c4py01467g.
[12] A. Jędrzak, B.F. Grześkowiak, K. Golba, E. Coy, K. Synoradzki, S. Jurga, T. Jesionowski, R. Mrówczyński, Magnetite nanoparticles and spheres for chemo- and photothermal therapy of hepatocellular carcinoma in vitro, Int. J. Nanomed. 15 (2020) 7923–7936, https://doi.org/10.2147/IJN.S257142.
[13] G. Loget, J.E. Yoo, A. Mazare, L. Wang, P. Schmuki, Highly controlled coating of biomimetic polydopamine in TiO2 nanotubes, Electrochem. Commun. 52 (2015) 41–44, https://doi.org/10.1016/j.elecom.2015.01.011.
[14] Y. Kim, E. Coy, H. Kim, R. Mrówczyński, P. Torruella, D.W. Jeong, K.S. Choi, J. H. Jang, M.Y. Song, D.J. Jang, F. Peiro, S. Jurga, H.J. Kim, Efficient photocatalytic production of hydrogen by exploiting the polydopamine-semiconductor interface, Appl. Catal. B Environ. 280 (2021) 119423, https://doi.org/10.1016/j.apcatb.2020.119423.

[15] M. Ruan, D. Guo, Q. Jia, A uniformly decorated and photostable polydopamine–organic semiconductor to boost the photoelectrochemical water splitting performance of CdS photoanodes, Dalt. Trans. 50 (2021) 1913–1922, https://doi.org/10.1039/d0dt04056h.

[16] D. Aguilar-Ferrer, T. Vasileiadis, I. Iatsunskyi, M. Ziółek, K. Żebrowska, O. Ivashchenko, P. Błaszkiewicz, B. Grześkowiak, R. Pazos, S. Moya, M. Bechelany, E. Coy, Understanding the photothermal and photocatalytic mechanism of polydopamine coated gold nanorods, Adv. Funct. Mater. 33 (2023) 2304208. https://doi.org/10.1002/adfm.202304208.

[17] A. Olejnik, K. Polaczek, M. Szkodo, A. Stanisławska, J. Ryl, K. Siuzdak, Laser-induced graphitization of polydopamine on titania nanotubes, ACS Appl. Mater. Interfaces. 15 (2023) 52921–52938, https://doi.org/10.1021/acsami.3c11580.

[18] M.J. Bigaj-Józefowska, E. Coy, K. Załęski, T. Zalewski, M. Grabowska, K. Jaskot, P. Perrigue, R. Mrówczyński, B.F. Grześkowiak, Biomimetic theranostic nanoparticles for effective anticancer therapy and MRI imaging, J. Photochem. Photobiol. B Biol. 249 (2023) 112813. https://doi.org/10.1016/j.jphotobiol.2023.112813.

[19] C. Cheng, S. Li, J. Zhao, X. Li, Z. Liu, L. Ma, X. Zhang, S. Sun, C. Zhao, Biomimetic assembly of polydopamine-layer on graphene: Mechanisms, versatile 2D and 3D architectures and pollutant disposal, Chem. Eng. J. 228 (2013) 468–481, https://doi.org/10.1016/j.cej.2013.05.019.

[20] Z. Xu, N. Wang, P. Liu, Y. Sun, Y. Wang, F. Fei, S. Zhang, J. Zheng, B. Han, Poly (dopamine) coating on 3D-printed poly-lactic-co-glycolic acid/β-tricalcium phosphate scaffolds for bone tissue engineering, Molecules. 24 (2019) 4397, https://doi.org/10.3390/molecules24234397.

[21] J.L. Chakka, T. Acri, N.Z. Laird, L. Zhong, K. Shin, S. Elangovan, A.K. Salem, Polydopamine functionalized VEGF gene-activated 3D printed scaffolds for bone regeneration, RSC Adv. 11 (2021) 13282–13291, https://doi.org/10.1039/d1ra01193f.

[22] J. Svoboda, M. Král, M. Dendisová, P. Matějka, O. Pop-Georgievsk, Unraveling the influence of substrate on the growth rate, morphology and covalent structure of surface adherent polydopamine films, Colloids Surf. B Biointerf. 205 (2021) 111897, https://doi.org/10.1016/j.colsurfb.2021.111897.

[23] F. Ponzio, P. Payamyar, A. Schneider, M. Winterhalter, J. Bour, F. Addiego, M. P. Krafft, J. Hemmerle, V. Ball, Polydopamine films from the forgotten air/water interface, J. Phys. Chem. Lett. 5 (2014) 3436–3440, https://doi.org/10.1021/jz501842r.

[24] F. Ponzio, V. Ball, Polydopamine deposition at fluid interfaces, Polym. Int. 65 (2016) 1251–1257, https://doi.org/10.1002/pi.5124.

[25] O.Y. Milyaeva, A.G. Bykov, R.A. Campbell, G. Loglio, R. Miller, B.A. Noskov, Polydopamine layer formation at the liquid – gas interface, Colloids Surfaces A Physicochem. Eng. Asp. 579 (2019) 123637, https://doi.org/10.1016/j.colsurfa.2019.123637.

[26] E. Coy, I. Iatsunskyi, J.C. Colmenares, Y. Kim, R. Mrówczyński, Polydopamine films with 2D-like layered structure and high mechanical resilience, ACS Appl. Mater. Interfaces. 13 (2021) 23113–23120, https://doi.org/10.1021/acsami.1c02483.

[27] J. Szewczyk, M. Pochylski, K. Szutkowski, M. Kempiński, R. Mrówczyński, I. Iatsunskyi, J. Gapiński, E. Coy, In-situ thickness control of centimetre-scale 2D-Like polydopamine films with large scalability, Mater. Today Chem. 24 (2022) 100935. https://doi.org/10.1016/j.mtchem.2022.100935.

[28] J. Szewczyk, V. Babacic, A. Krysztofik, O. Ivashchenko, M. Pochylski, R. Pietrzak, J. Gapiński, B. Graczykowski, M. Bechelany, E. Coy, Control of intermolecular interactions toward the production of free-standing interfacial polydopamine films, ACS Appl. Mater. Interfaces. 15 (2023) 36922–36935, https://doi.org/10.1021/acsami.3c05236.

[29] S. Hong, C.F. Schaber, K. Dening, E. Appel, S.N. Gorb, H. Lee, Air/water interfacial formation of freestanding, stimuli-responsive, self-healing catecholamine janus-faced microfilms, Adv. Mater. 26 (2014) 7581–7587, https://doi.org/10.1002/adma.201403259.

[30] B.N. Ren, H.H. Pi, Y.S. Gu, R. Wang, X.Q. Zhang, J. Wu, Research progress in preparation and application of Janus membranes, Cailiao Gongcheng/J. Mater. Eng. 48 (2020) 72–80. https://doi.org/10.11868/j.issn.1001-4381.2019.000530.

[31] D. Aguilar-Ferrer, J. Szewczyk, E. Coy, Recent developments in polydopamine-based photocatalytic nanocomposites for energy production: physico-chemical properties and perspectives, Catal. Today. 397–399 (2022) 316–349, https://doi.org/10.1016/j.cattod.2021.08.016.

[32] S.N. Ahmed, W. Haider, Heterogeneous photocatalysis and its potential applications in water and wastewater treatment: A review, Nanotechnology. 29 (2018) 342001, https://doi.org/10.1088/1361-6528/aac6ea.

[33] V. Fedorenko, R. Viter, R. Mrówczyński, D. Damberga, E. Coy, I. Iatsunskyi, Synthesis and photoluminescence properties of hybrid 1D core–shell structured nanocomposites based on ZnO/polydopamine, RSC Adv. 10 (2020) 29751–29758, https://doi.org/10.1039/D0RA04829A.

[34] D. Damberga, V. Fedorenko, K. Grundšteins, Ş. Altundal, A. Šutka, A. Ramanavičius, E. Coy, R. Mrówczyński, I. Iatsunskyi, R. Viter, Influence of pda coating on the structural, optical and surface properties of zno nanostructures, Nanomaterials. 10 (2020) 1–11, https://doi.org/10.3390/nano10122438.

[35] X. Sun, L. Yan, R. Xu, M. Xu, Y. Zhu, Surface modification of TiO 2 with polydopamine and its effect on photocatalytic degradation mechanism, Colloids Surfaces A Physicochem. Eng. Asp. 570 (2019) 199–209, https://doi.org/10.1016/j.colsurfa.2019.03.018.

[36] L. Wang, J. Zhang, H. Yu, I.H. Patir, Y. Li, S. Wageh, A.A. Al-Ghamdi, J. Yu, Dynamics of photogenerated charge carriers in inorganic/organic s-scheme heterojunctions, J. Phys. Chem. Lett. 13 (2022) 4695–4700, https://doi.org/10.1021/acs.jpclett.2c01332.

[37] I. Khan, K. Saeed, I. Zekker, B. Zhang, A.H. Hendi, A. Ahmad, S. Ahmad, N. Zada, H. Ahmad, L.A. Shah, T. Shah, I. Khan, Review on methylene blue: its properties, uses, toxicity and photodegradation, Water (switzerland). 14 (2022) 242, https://doi.org/10.3390/w14020242.

[38] D. Liu, C. Li, C. Zhao, Q. Zhao, T. Niu, L. Pan, P. Xu, F. Zhang, W. Wu, T. Ni, Facile synthesis of three-dimensional hollow porous carbon doped polymeric carbon nitride with highly efficient photocatalytic performance, Chem. Eng. J. 438 (2022) 135623, https://doi.org/10.1016/j.cej.2022.135623.

[39] D. Liu, H. Li, R. Gao, Q. Zhao, Z. Yang, X. Gao, Z. Wang, F. Zhang, W. Wu, Enhanced visible light photoelectrocatalytic degradation of tetracycline hydrochloride by I and P co-doped TiO2 photoelectrode, J. Hazard. Mater. 406 (2021) 124309, https://doi.org/10.1016/j.jhazmat.2020.124309.

[40] D. Liu, C. Li, J. Ge, C. Zhao, Q. Zhao, F. Zhang, T. Ni, W. Wu, 3D interconnected g-C3N4 hybridized with 2D Ti3C2 MXene nanosheets for enhancing visible light photocatalytic hydrogen evolution and dye contaminant elimination, Appl. Surf. Sci. 579 (2022) 152180, https://doi.org/10.1016/j.apsusc.2021.152180.

[41] U. Chakraborty, G. Kaur, H.-G. Rubahn, A. Kaushik, G.R. Chaudhary, Y.K. Mishra, Advanced metal oxides nanostructures to recognize and eradicate water pollutants, Prog. Mater. Sci. 139 (2023) 101169. https://doi.org/10.1016/j.pmatsci.2023.101169.

[42] N. Vogel, S. Goerres, K. Landfester, C.K. Weiss, A convenient method to produce close- and non-close-packed monolayers using direct assembly at the air-water interface and subsequent plasma-induced size reduction, Macromol. Chem. Phys. 212 (2011) 1719–1734, https://doi.org/10.1002/macp.201100187.

[43] M. Moret, A. Abou Chaaya, M. Bechelany, P. Miele, Y. Robin, O. Briot, Atomic Layer Deposition of zinc oxide for solar cell applications, Superlatt. Microstruct. 75 (2014) 477–484, https://doi.org/10.1016/j.spmi.2014.07.050.

[44] I. Iatsunskyi, M. Jancelewicz, G. Nowaczyk, M. Kempiński, B. Peplińska, M. Jarek, K. Załęski, S. Jurga, V. Smyntyna, Atomic layer deposition TiO2 coated porous silicon surface: structural characterization and morphological features, Thin Solid Films. 589 (2015) 303–308, https://doi.org/10.1016/j.tsf.2015.05.056.

[45] A.A. Chaaya, R. Viter, M. Bechelany, Z. Alute, D. Erts, A. Zalesskaya, K. Kovalevskis, V. Rouessac, V. Smyntyna, P. Miele, Evolution of microstructure and related optical properties of ZnO grown by atomic layer deposition, Beilstein J. Nanotechnol. 4 (2013) 690–698, https://doi.org/10.3762/bjnano.4.78.

[46] D. Nečas, P. Klapetek, Gwyddion: an open-source software for SPM data analysis, Cent. Eur. J. Phys. 10 (2012) 181–188, https://doi.org/10.2478/s11534-011-0096-2.

[47] P. Makuła, M. Pacia, W. Macyk, How To correctly determine the band gap energy of modified semiconductor photocatalysts based on UV-Vis spectra, J. Phys. Chem. Lett. 9 (2018) 6814–6817, https://doi.org/10.1021/acs.jpclett.8b02892.

[48] E. Coy, K. Siuzdak, I. Grądzka-Kurzaj, S. Sayegh, M. Weber, M. Ziółek, M. Bechelany, I. Iatsunskyi, Exploring the effect of BN and B-N bridges on the photocatalytic performance of semiconductor heterojunctions: Enhancing carrier transfer mechanism, Appl. Mater. Today. 24 (2021) 101095, https://doi.org/10.1016/j.apmt.2021.101095.

[49] J. Idĭgoras, G. Burdzinski, J. Karolczak, J. Kubicki, G. Oskam, J.A. Anta, M. Ziółek, The impact of the electrical nature of the metal oxide on the performance in dye-sensitized solar cells: new look at old paradigms, J. Phys. Chem. c. 119 (2015) 3931–3944, https://doi.org/10.1021/jp512330f.

[50] J.C. Foster, I. Akar, M.C. Grocott, A.K. Pearce, R.T. Mathers, R.K. O'Reilly, 100th anniversary of macromolecular science viewpoint: the role of hydrophobicity in polymer phenomena, ACS Macro Lett. 9 (2020) 1700–1707, https://doi.org/10.1021/acsmacrolett.0c00645.

[51] S. Neyshtadt, J.P. Jahnke, R.J. Messinger, A. Rawal, T. Segal Peretz, D. Huppert, B.F. Chmelka, G.L. Frey, Understanding and controlling organic - Inorganic interfaces in mesostructured hybrid photovoltaic materials, J. Am. Chem. Soc. 133 (2011) 10119–10133, https://doi.org/10.1021/ja200054z.

[52] H. Hemmatpour, O. De Luca, D. Crestani, M.C.A. Stuart, A. Lasorsa, P.C.A. van der Wel, K. Loos, T. Giousis, V. Haddadi-Asl, P. Rudolf, New insights in polydopamine formation via surface adsorption, Nat. Commun. 14 (2023) 664, https://doi.org/10.1038/s41467-023-36303-8.

[53] F. Morteo-Flores, A. Roldan, The effect of pristine and hydroxylated oxide surfaces on the guaiacol HDO process: a DFT study, ChemPhysChem. 23 (2022) 1, https://doi.org/10.1002/cphc.202100583.

[54] Y. Mai, A. Eisenberg, Self-assembly of block copolymers, Chem. Soc. Rev. 41 (2012) 5969–5985, https://doi.org/10.1039/c2cs35115c.

[55] Y.O. Kim, J.M. You, H.S. Jang, S.K. Choi, B.Y. Jung, O. Kang, J.W. Kim, Y.S. Lee, Eumelanin as a support for efficient palladium nanoparticle catalyst for Suzuki coupling reaction of aryl chlorides in water, Tetrahedron Lett. 58 (2017) 2149–2152, https://doi.org/10.1016/j.tetlet.2017.04.062.

[56] T. Ami, M. Suzuki, MOCVD growth of (100)-oriented CeO2 thin films on hydrogen-terminated Si(100) substrates, Mater. Sci. Eng. b. 54 (1998) 84–91, https://doi.org/10.1016/s0921-5107(98)00133-0.

[57] Z. Tian, W. Hwang, Y.J. Kim, Mechanistic understanding of monovalent cation transport in eumelanin pigments, J. Mater. Chem. b. 7 (2019) 6355–6361, https://doi.org/10.1039/C9TB01211G.

[58] N. Rono, J.K. Kibet, B.S. Martincigh, V.O. Nyamori, A review of the current status of graphitic carbon nitride, Crit. Rev. Solid State Mater. Sci. 46 (2021) 189–217, https://doi.org/10.1080/10408436.2019.1709414.

[59] B. Gurzęda, A. Subrati, P. Florczak, Z. Kabacińska, T. Buchwald, L. Smardz, B. Peplińska, S. Jurga, P. Krawczyk, Two-step synthesis of well-ordered layered graphite oxide with high oxidation degree, Appl. Surf. Sci. 507 (2020) 145049, https://doi.org/10.1016/j.apsusc.2019.145049.

[60] A. Subrati, S. Mondal, M. Ali, A. Alhindi, R. Ghazi, A. Abdala, D. Reinalda, S. Alhassan, Developing hydrophobic graphene foam for oil spill cleanup, Ind.

Eng. Chem. Res. 56 (2017) 6945–6951, https://doi.org/10.1021/acs.iecr.7b00716.
[61] F.T. Johra, J.W. Lee, W.G. Jung, Facile and safe graphene preparation on solution based platform, J. Ind. Eng. Chem. 20 (2014) 2883–2887, https://doi.org/10.1016/j.jiec.2013.11.022.
[62] T. Qiu, J.G. Yang, X.J. Bai, Y.L. Wang, The preparation of synthetic graphite materials with hierarchical pores from lignite by one-step impregnation and their characterization as dye absorbents, RSC Adv. 9 (2019) 12737–12746, https://doi.org/10.1039/c9ra00343f.
[63] S. Sedira, B. Mendaci, Hydrothermal synthesis of spherical carbon nanoparticles (CNPs) for supercapacitor electrodes uses, Mater. Renew. Sustain Energy. 9 (2020) 1–9, https://doi.org/10.1007/s40243-019-0161-0.
[64] N. Cao, Y. Zhang, Study of reduced graphene oxide preparation by hummers' method and related characterization, J. Nanomater. 2015 (2015) 1–5, https://doi.org/10.1155/2015/168125.
[65] M. Kyotani, K. Hiratani, T. Okada, S. Matsushita, K. Akagi, Preparation of 2D carbon materials by chemical carbonization of cellulosic materials to avoid thermal decomposition, Glob. Challenges. 1 (2017) 1700061, https://doi.org/10.1002/gch2.201700061.
[66] R. Tejido-Rastrilla, G. Baldi, A.R. Boccaccini, Ag containing polydopamine coating on a melt-derived bioactive glass-ceramic: effect on surface reactivity, Ceram. Int. 44 (2018) 16083–16087, https://doi.org/10.1016/j.ceramint.2018.05.198.
[67] H. Li, J. Xi, A.G. Donaghue, J. Keum, Y. Zhao, K. An, E.R. McKenzie, F. Ren, Synthesis and catalytic performance of polydopamine supported metal nanoparticles, Sci. Rep. 10 (2020) 10416, https://doi.org/10.1038/s41598-020-67458-9.
[68] A.C. Ferrari, Raman spectroscopy of graphene and graphite: Disorder, electron-phonon coupling, doping and nonadiabatic effects, Solid State Commun. 143 (2007) 47–57, https://doi.org/10.1016/j.ssc.2007.03.052.
[69] C. Silva, F. Simon, P. Friedel, P. Pötschke, C. Zimmerer, Elucidating the chemistry behind the reduction of graphene oxide using a green approach with polydopamine, Nanomaterials. 9 (2019) 902, https://doi.org/10.3390/nano9060902.
[70] P. Venezuela, M. Lazzeri, F. Mauri, Theory of double-resonant Raman spectra in graphene: intensity and line shape of defect-induced and two-phonon bands, Phys. Rev. B - Condens. Matter Mater. Phys. 84 (2011) 035433, https://doi.org/10.1103/PhysRevB.84.035433.
[71] C. Pardanaud, G. Cartry, L. Lajaunie, R. Arenal, J.G. Buijnsters, Investigating the possible origin of raman bands in defective sp2/sp3 carbons below 900 cm−1: phonon density of states or double resonance mechanism at play? C — J. Carbon Res. 5 (2019) 79, https://doi.org/10.3390/c5040079.
[72] J. Campos-Delgado, L.G. Cançado, C.A. Achete, A. Jorio, J.P. Raskin, Raman scattering study of the phonon dispersion in twisted bilayer graphene, Nano Res. 6 (2013) 269–274, https://doi.org/10.1007/s12274-013-0304-z.
[73] D. Roy, M. Chhowalla, H. Wang, N. Sano, I. Alexandrou, T.W. Clyne, G.A. J. Amaratunga, Characterisation of carbon nano-onions using Raman spectroscopy, Chem. Phys. Lett. 373 (2003) 52–56, https://doi.org/10.1016/S0009-2614(03)00523-2.
[74] G. Perna, M. Lasalvia, V. Capozzi, Vibrational spectroscopy of synthetic and natural eumelanin, Polym. Int. 65 (2016) 1323–1330, https://doi.org/10.1002/pi.5182.
[75] J. Liebscher, R. Mrówczyński, H.A. Scheidt, C. Filip, N.D. Haìdade, R. Turcu, A. Bende, S. Beck, Structure of polydopamine: a never-ending story? Langmuir. 29 (2013) 10539–10548, https://doi.org/10.1021/la4020288.
[76] A. Alkhouzaam, H. Qiblawey, M. Khraisheh, Polydopamine functionalized graphene oxide as membrane nanofiller: Spectral and structural studies, Membranes. 11 (2021) 1–17, https://doi.org/10.3390/membranes11020086.
[77] T. Touqeer, M.W. Mumtaz, H. Mukhtar, A. Irfan, S. Akram, A. Shabbir, U. Rashid, I.A. Nehdi, T.S. Yaw Choong, Fe3O4-PDA-lipase as surface functionalized nano biocatalyst for the production of biodiesel using waste cooking oil as feedstock: characterization and process optimization, Energies. 13 (2020) 177, https://doi.org/10.3390/en13010177.
[78] H. Luo, C. Gu, W. Zheng, F. Dai, X. Wang, Z. Zheng, Facile synthesis of novel size-controlled antibacterial hybrid spheres using silver nanoparticles loaded with poly-dopamine spheres, RSC Adv. 5 (2015) 13470–13477, https://doi.org/10.1039/c4ra16469e.
[79] M. Liu, W. Jiang, Q. Chen, S. Wang, Y. Mao, X. Gong, K.C.F. Leung, J. Tian, H. Wang, S. Xuan, A facile one-step method to synthesize SiO2@polydopamine core–shell nanospheres for shear thickening fluid, RSC Adv. 6 (2016) 29279–29287, https://doi.org/10.1039/c5ra25759j.
[80] M. Massaro, V. Campisciano, C.V. Iborra, L.F. Liotta, M. Sánchez-Polo, S. Riela, M. Gruttadauria, New mussel inspired polydopamine-like silica-based material for dye adsorption, Nanomaterials. 10 (2020) 1–12, https://doi.org/10.3390/nano10071416.
[81] M. Kehrer, J. Duchoslav, A. Hinterreiter, M. Cobet, A. Mehic, T. Stehrer, D. Stifter, XPS investigation on the reactivity of surface imine groups with TFAA, Plasma Process. Polym. 16 (2019) 1800160, https://doi.org/10.1002/ppap.201800160.
[82] Q. Wei, F. Zhang, J. Li, B. Li, C. Zhao, Oxidant-induced dopamine polymerization for multifunctional coatings, Polym. Chem. 1 (2010) 1430–1433, https://doi.org/10.1039/c0py00215a.
[83] W. Shan, W. Walukiewicz, J.W. Ager, K.M. Yu, H.B. Yuan, H.P. Xin, G. Cantwell, J.J. Song, Nature of room-temperature photoluminescence in ZnO, Appl. Phys. Lett. 86 (2005) 1–3, https://doi.org/10.1063/1.1923757.
[84] A. Galdámez-Martinez, G. Santana, F. Güell, P.R. Martínez-Alanis, A. Dutt, Photoluminescence of zno nanowires: a review, Nanomaterials. 10 (2020) 857, https://doi.org/10.3390/nano10050857.
[85] A.B. Djurišić, Y.H. Leung, Optical properties of ZnO nanostructures, Small. 2 (2006) 944–961, https://doi.org/10.1002/smll.200600134.
[86] C.H. Chia, J.N. Chen, T.C. Han, J.W. Chiou, Y.C. Lin, W.L. Hsu, W.C. Chou, Size dependence of exciton-phonon coupling in sol-gel ZnMgO powders, J. Appl. Phys. 109 (2011) 063526, https://doi.org/10.1063/1.3563574.
[87] M. Xiao, M.D. Shawkey, A. Dhinojwala, Bioinspired melanin-based optically active materials, Adv. Opt. Mater. 8 (2020) 1–15, https://doi.org/10.1002/adom.202000932.
[88] F. Rahman, Zinc oxide light-emitting diodes: a review, Opt. Eng. 58 (2019) 1, https://doi.org/10.1117/1.oe.58.1.010901.
[89] T.J. Bruno, P.D.N. Svoronos, CRC Handbook of Fundamental Spectroscopic Correlation Charts (2005), https://doi.org/10.1201/9780849332500.
[90] F. Fabbri, M. Villani, A. Catellani, A. Calzolari, G. Cicero, D. Calestani, G. Calestani, A. Zappettini, B. Dierre, T. Sekiguchi, G. Salviati, Zn vacancy induced green luminescence on non-polar surfaces in ZnO nanostructures, Sci. Rep. 4 (2014) 5158, https://doi.org/10.1038/srep05158.
[91] N.H. Alvi, K. ul Hasan, O. Nur, M. Willander, The origin of the red emission in n-zno nanotubes/p-gan white light emitting diodes, Nanoscale Res. Lett. 6 (2011) 130, https://doi.org/10.1186/1556-276X-6-130.
[92] A. Janotti, C.G. Van De Walle, Native point defects in ZnO, Phys. Rev. B - Condens. Matter Mater. Phys. 76 (2007) 165202, https://doi.org/10.1103/PhysRevB.76.165202.
[93] R. Raji, K.G. Gopchandran, ZnO nanostructures with tunable visible luminescence: effects of kinetics of chemical reduction and annealing, J. Sci. Adv. Mater. Dev. 2 (2017) 51–58, https://doi.org/10.1016/j.jsamd.2017.02.002.
[94] Ü. Özgür, Y.I. Alivov, C. Liu, A. Teke, M.A. Reshchikov, S. Doğan, V. Avrutin, S. J. Cho, H. Morko, A comprehensive review of ZnO materials and devices, J. Appl. Phys. 98 (2005) 1–103, https://doi.org/10.1063/1.1992666.
[95] S.A. Studenikin, N. Golego, M. Cocivera, Fabrication of green and orange photoluminescent, undoped ZnO films using spray pyrolysis, J. Appl. Phys. 84 (1998) 2287–2294, https://doi.org/10.1063/1.368295.
[96] X. Wang, A. Kafizas, X. Li, S.J.A. Moniz, P.J.T. Reardon, J. Tang, I.P. Parkin, J. R. Durrant, Transient absorption spectroscopy of anatase and rutile: The impact of morphology and phase on photocatalytic activity, J. Phys. Chem. c. 119 (2015) 10439–10447, https://doi.org/10.1021/acs.jpcc.5b01858.
[97] Y. Tamaki, A. Furube, R. Katoh, M. Murai, K. Hara, H. Arakawa, M. Tachiya, Trapping dynamics of electrons and holes in a nanocrystalline TiO2 film revealed by femtosecond visible/near-infrared transient absorption spectroscopy, Comptes Rend. Chim. 9 (2006) 268–274, https://doi.org/10.1016/j.crci.2005.05.018.
[98] A. Furube, T. Asahi, H. Masuhara, H. Yamashita, M. Anpo, Charge carrier dynamics of standard TiO2 catalysts revealed by femtosecond diffuse reflectance spectroscopy, J. Phys. Chem. b. 103 (1999) 3120–3127, https://doi.org/10.1021/jp984162h.
[99] X. Yang, N. Tamai, How fast is interfacial hole transfer? In situ monitoring of carrier dynamics in anatase TiO2 nanoparticles by femtosecond laser spectroscopy, Phys. Chem. Chem. Phys. 3 (2001) 3393–3398, https://doi.org/10.1039/b101721g.
[100] G. Mattioli, P. Alippi, F. Filippone, R. Caminiti, A. Amore Bonapasta, Deep versus shallow behavior of intrinsic defects in rutile and anatase TiO2 polymorphs, J. Phys. Chem. c. 114 (2010) 21694–21704, https://doi.org/10.1021/jp1041316.
[101] G. Mattioli, F. Filippone, P. Alippi, A. Amore Bonapasta, Ab initio study of the electronic states induced by oxygen vacancies in rutile and anatase TiO2, Phys. Rev. B - Condens. Matter Mater. Phys. 78 (2008) 241201, https://doi.org/10.1103/PhysRevB.78.241201.
[102] W.J. Yin, B. Wen, C. Zhou, A. Selloni, L.M. Liu, Excess electrons in reduced rutile and anatase TiO2, Surf. Sci. Rep. 73 (2018) 58–82, https://doi.org/10.1016/j.surfrep.2018.02.003.
[103] C. Koral, M. Fantauzzi, C. Imparato, G.P. Papari, B. Silvestri, A. Aronne, A. Andreone, A. Rossi, Defects in the amorphous−crystalline evolution of gel-derived TiO2, J. Phys. Chem. c. 124 (2020) 23773–23783, https://doi.org/10.1021/acs.jpcc.0c07568.
[104] T. Berger, O. Diwald, E. Knözinger, M. Sterrer, J.T. Yates, UV induced local heating effects in TiO2 nanocrystals, Phys. Chem. Chem. Phys. 8 (2006) 1822–1826, https://doi.org/10.1039/b517107e.
[105] X. Wang, Z. Feng, J. Shi, G. Jia, S. Shen, J. Zhou, C. Li, Trap states and carrier dynamics of TiO2 studied by photoluminescence spectroscopy under weak excitation condition, Phys. Chem. Chem. Phys. 12 (2010) 7083–7090, https://doi.org/10.1039/b925277k.
[106] K.E. Knowles, M.D. Koch, J.L. Shelton, Three applications of ultrafast transient absorption spectroscopy of semiconductor thin films: spectroelectrochemistry, microscopy, and identification of thermal contributions, J. Mater. Chem. c. 6 (2018) 11853–11867, https://doi.org/10.1039/c8tc02977f.
[107] W. Xu, W. Yang, H. Guo, L. Ge, J. Tu, C. Zhen, Constructing a TiO2/PDA core/shell nanorod array electrode as a highly sensitive and stable photoelectrochemical glucose biosensor, RSC Adv. 10 (2020) 10017–10022, https://doi.org/10.1039/c9ra10445c.
[108] K. Mistewicz, Pyroelectric nanogenerator based on an SbSI–TiO2 nanocomposite, Sensors. 22 (2022) 69, https://doi.org/10.3390/s22010069.
[109] Z. Wang, R. Yu, X. Wang, W. Wu, Z.L. Wang, Ultrafast response p-Si/n-ZnO heterojunction ultraviolet detector based on pyro-phototronic effect, Adv. Mater. 28 (2016) 6880–6886, https://doi.org/10.1002/adma.201600884.

[110] Z. Wang, R. Yu, C. Pan, Z. Li, J. Yang, F. Yi, Z.L. Wang, Light-induced pyroelectric effect as an effective approach for ultrafast ultraviolet nanosensing, Nat. Commun. 6 (2015) 8401, https://doi.org/10.1038/ncomms9401.
[111] K. Zhao, B. Ouyang, Y. Yang, Enhancing photocurrent of radially polarized ferroelectric BaTiO3 materials by ferro-pyro-phototronic effect, Iscience. 3 (2018) 208–216, https://doi.org/10.1016/j.isci.2018.04.016.
[112] J.M. Atkin, D. Song, T.M. Shaw, E. Cartier, R.B. Laibowitz, T.F. Heinz, Photocurrent spectroscopy of low- k dielectric materials: Barrier heights and trap densities, J. Appl. Phys. 103 (2008) 094104, https://doi.org/10.1063/1.2907958.
[113] H.H. Pham, L.W. Wang, Oxygen vacancy and hole conduction in amorphous TiO2, Phys. Chem. Chem. Phys. 17 (2015) 541–550, https://doi.org/10.1039/c4cp04209c.
[114] M.J. Zhao, Z.T. Sun, Z.X. Zhang, X.P. Geng, W.Y. Wu, S.Y. Lien, W.Z. Zhu, Suppression of oxygen vacancy defects in sALD-ZnO films annealed in different conditions, Materials (basel). 13 (2020) 3910, https://doi.org/10.3390/ma13183910.
[115] N. Ahmad, X. Zhang, S. Yang, D. Zhang, J. Wang, S.U. Zafar, Y. Li, Y. Zhang, S. Hussain, Z. Cheng, A. Kumaresan, H. Zhou, Polydopamine/ZnO electron transport layers enhance charge extraction in inverted non-fullerene organic solar cells, J. Mater. Chem. c. 7 (2019) 10795–10801, https://doi.org/10.1039/c9tc02781e.
[116] Z. Wang, F. Tang, H. Fan, L. Wang, Z. Jin, Polydopamine generates hydroxyl free radicals under ultraviolet-light illumination, Langmuir. 33 (2017) 5938–5946, https://doi.org/10.1021/acs.langmuir.7b01065.
[117] C.S. Tan, Y. Zhao, R.H. Guo, W.T. Chuang, L.J. Chen, M.H. Huang, Facet-dependent surface trap states and carrier lifetimes of silicon, Nano Lett. 20 (2020) 1952–1958, https://doi.org/10.1021/acs.nanolett.9b05237.